Vascular Progenitors Generated from Tankyrase Inhibitor-Regulated Diabetic Induced Pluripotent Stem Cells Potentiate Efficient Revascularization of Ischemic Retina

Tea Soon Park[1], Ludovic Zimmerlin[1], Rebecca Evans-Moses[1], Justin Thomas[1], Jeffrey S. Huo[1], Riya Kanherkar[1], Alice He[1], Nensi Ruzgar[1], Schuyler Metzger[1], Rhonda Grebe[2], Imran Bhutto[2], Gerard Lutty[2], Elias T. Zambidis[1*]

Institute for Cell Engineering, Department of Oncology[1], and Wilmer Eye Institute[2], The Johns Hopkins School of Medicine, Baltimore, MD USA

Key words

pluripotency, human pluripotent stem cell, differentiation, vascular progenitors, diabetes, cell therapy, ischemic retinopathy

*Correspondence: Elias T. Zambidis, MD, PhD
Institute for Cell Engineering, and
Sidney Kimmel Comprehensive Cancer Center,
The Johns Hopkins University School of Medicine
733 N. Broadway, MRB 755, Baltimore, MD 21205

ABSTRACT

Vascular regenerative therapies with conventional human induced pluripotent stem cells (hiPSC) currently remain limited by high interline variability of differentiation and poor efficiency for generating functionally transplantable vascular progenitors (VP). Here, we report the advantage of a new class of tankyrase inhibitor-regulated naïve hiPSC (N-hiPSC) for significantly improving vascular cell therapies. Conventional hiPSC reprogrammed from type-1 diabetic donor fibroblasts (DhiPSC) were stably reverted to N-hiPSC with a cocktail of LIF and three small molecules inhibiting the tankyrase, MEK, and GSK3β signaling pathways (LIF-3i). Naïve diabetic hiPSC (N-DhiPSC) possessed higher functional pluripotency, higher proliferation, decreased lineage priming, and more stable genomic integrity than conventional DhiPSC. VP differentiated from N-DhiPSC expanded more efficiently, and displayed higher *in vitro* vascular functionality than VP from isogenic conventional DhiPSC cultures. Moreover, N-DhiPSC-derived VP survived, migrated, and engrafted *in vivo* into the deep vasculature of the neural retinal layers with significantly higher efficiencies than isogenic primed D-hiPSC-VP in a murine model of ischemic retinopathy. Epigenetic analyses of CpG DNA methylation and histone configurations at developmental promoters of N-hiPSC revealed tight regulation of lineage-specific gene expression and a de-repressed naïve epiblast-like epigenetic state that was highly poised for multi-lineage transcriptional activation. We propose that autologous or cell-banked vascular/pericytic progenitors derived from tankyrase inhibitor-regulated N-hiPSC will more effectively reverse the pathology that drives vascular disorders such as diabetic retinopathy.

INTRODUCTION

The human retina is dependent on an intact, functional vasculature. If either the retinal or choroidal vasculature become compromised, neurons and supporting cells in ischemic areas rapidly die. During progressive diabetic retinopathy (DR), ischemic death of retinal pericytes and endothelial cells [1-4] leads to acellular vascular segments, rapid death of retinal neurons, microglial stimulation, secondary inflammation, macular edema, and subsequent retinal damage from proliferative neovascularization [5,6]. If acellular retinal capillaries could be regenerated with patient-specific cellular therapies, neuronal death and pathological neovascularization could be halted or reversed. Human induced pluripotent stem cell (hiPSC) cell therapies offer a versatile patient-specific approach for *de novo* regeneration of pericytic-endothelial cells [7,8]. Durable, albeit limited long-term *in vivo* engraftment of conventional hiPSC-derived vascular progenitor (VP) cells into the ischemic retina was previously reported [7]. However, despite the potential and rapid advance of ocular regenerative medicine [9,10], conventional hiPSC lines currently remain limited by highly variable differentiation efficiency and poor *in vivo* functionality of VP derived from them.

One critical variable impacting the differentiation efficiency and functional pluripotency of conventional hiPSC is the developmental, biochemical, and epigenetic commonality of hiPSC with 'primed' murine post-implantation epiblast stem cells (mEpiSC), which possess a more restricted pluripotency than inner cell mass-derived mouse ESC (mESC) (Reviewed in [11]). Conventional hiPSC cultures adopt a spectrum of mEpiSC-like pluripotent states with highly variable lineage-primed gene expressions and post-implantation primed epiblast epigenetic marks that result in inconsistent or diminished differentiation [12,13]. Moreover, epigenetic aberrations in diseased states such as diabetes may further inhibit efficient donor cell reprogramming to functional pluripotent states [14-18].

Naïve hiPSC (N-hiPSC) with more primitive pre-implantation epiblast phenotypes, decreased lineage priming, improved epigenetic stability, and higher functionality of differentiated progenitors may solve these obstacles, but this potential has not yet been demonstrated. Several groups have reported various complex small molecule approaches that putatively captured human 'naïve-like' pluripotent molecular states that are more primitive than those exhibited by conventional, primed hiPSC (reviewed in [11]). However, many of these human

naïve-like states exhibited karyotypic instability, global loss of parental genomic imprinting, and impaired multi-lineage differentiation performance. In contrast, a small molecule-based reversion method that employed the tankyrase inhibitor XAV939 along with leukemia inhibitory factor (LIF), and the classic 2i cocktail of GSK3β and MEK/ERK inhibition (LIF-3i) avoided these caveats [12,13]. The LIF-3i method rapidly reverted conventional, lineage-primed human pluripotent stem cells (hPSC) to a stable pluripotent state that adopted biochemical, transcriptional, and epigenetic features of the human pre-implantation naïve epiblast. Interestingly, inclusion of XAV939 in various growth media has now identified a new class of pluripotent stem cells with either primed or naïve phenotypes. For example, tankyrase inhibition expanded the functionality of either murine PSC [19,20], or hESC with primed epiblast phenotypes [20,21], including conferred expanded potential for generating extra-embryonic derivatives [19,21].

Here, we demonstrate for the first time that the epigenetic obstacle of lineage priming and high interline variability of vascular lineage differentiation from normal and diseased conventional hiPSC was eliminated by reversion to this novel tankyrase inhibitor-regulated naïve pluripotent state. Notably, naive diabetic VP differentiated from naïve patient-specific diabetic hiPSC (DhiPSC) maintained greater genomic stability than isogenic conventional diabetic VP, higher expression of vascular identity markers, decreased non-lineage gene expression, and were superior in migrating to and re-vascularizing the deep neural layers of the ischemic retina. These N-hiPSC-derived VP will have great potential for treatment of vascular ischemic disorders. Moreover, we propose that reprogramming of patient donor cells to tankyrase inhibitor-regulated N-hiPSC may have wide impact in regenerative medicine by more effectively erasing dysfunctional epigenetic memory sustained from chronic diseased states such as diabetes.

RESULTS

LIF-3i naïve reversion of conventional hiPSC significantly improved their multi-lineage differentiation potency. Culture of conventional hiPSC with a small molecule cocktail of LIF, the tankyrase inhibitor XAV939, the GSK3β inhibitor CHIR99021, and the MEK inhibitor PD0325901 (LIF-3i) conferred a broad repertoire of hiPSC (**Table S1**) with molecular and

biochemical characteristics unique to naïve pluripotency, including increased phosphorylated STAT3 signaling, decreased ERK phosphorylation, global 5-methylcytosine CpG hypomethylation, genome-wide CpG demethylation at ESC-specific gene promoters, and dominant distal OCT4 enhancer usage [12,13]. LIF-3i-reverted N-hiPSC maintained normal karyotypes, and were devoid of systematic loss of imprinted CpG patterns or irreversible demethylation defects reported in other naïve reversion systems, and that were attributed to prolonged culture with MEK inhibitors [22-24] .

In contrast to reports of difficult, if not deficient, directed differentiations of human naïve states, or requirement for culture back to a primed state [25,26], LIF-3i-reverted N-hiPSC differentiated *directly* with significantly higher efficiencies and more rapid kinetics than their isogenic primed, conventional hiPSC counterparts, and did not require an additional 're-priming' culture step (**Fig. S1**). Moreover, LIF-3i reversion decreased lineage-primed gene expression, and diminished the interline variability of directed differentiation typically observed amongst independent primed, conventional hiPSC lines. For example, LIF-3i-reverted vs. primed, conventional hiPSC lines were differentiated in parallel in identical neural induction medium; N-hiPSC produced faster kinetics and 2 to 3-fold higher levels of $Nestin^{+}SOX1^{+}$, $Nestin^{+}PAX6^{+}$, and $MAP2^{+}$. Differentiated neural ectodermal progenitor cells also more efficiently terminally differentiated into elongated neurites expressing Tuj1 (**Fig. S1a**). Similarly, LIF-3i N-hiPSC vs their isogenic primed hiPSC counterparts were directly differentiated in parallel cultures into definitive endoderm; N-hiPSC generated higher quantities of $CXCR4^{+}SOX17^{+}FOXA2^{+}$ progenitors at levels surpassing their isogenic primed controls (**Fig. S1b**). LIF-3i N-hiPSC similarly differentiated more efficiently than isogenic primed hiPSC into vascular mesoderm (*e.g.,* $CD31^{+}CD146^{+}$, KDR^{+}, $CD140b^{+}$, $CD34^{+}$, and $CD143^{+}$ VP) regardless of hiPSC genetic background (*n*=6) (**Fig. S1c**).

To further validate the functional pluripotency of fibroblast-derived N-hiPSC, we investigated multi-lineage differentiation performance in teratoma assays (**Fig. 1**). Gross histological analysis of eight-week old teratomas from primed and naïve hiPSC cultures demonstrated that although both efficiently generated lineages of all three germ layers, there were marked quantitative differences between isogenic primed and LIF-3i-reverted fibroblast-hiPSC in generating teratoma organoid structures. Whereas primed hiPSC produced well-formed cystic teratomas with strong bias toward mesodermal cartilage differentiation (**Fig. 1b**), N-

hiPSC teratomas generated more homogenous and robust distribution of multiple structures from all three germ layer lineages, with significantly greater endodermal (gut structures), neuro-ectodermal (neural rosettes, retinal pigmented epithelial) structures, and mesodermal (cartilage) structures (**Fig. 1a,b**). LIF-3i fibroblast-hiPSC teratomas also retained proliferating organoid structures with significantly higher proliferative indices (*e.g.*, 30-50% $Ki67^+$ in $CK8^+$ gut endodermal, $NG2^+$ mesodermal cartilage structures) than their isogenic primed fibroblast-hiPSC counterpart (**Fig. 1c,d**).

Reprogramming of type-1 diabetic donor skin fibroblasts to conventional DhiPSC and subsequent reversion to N-DhiPSC. To test the therapeutic potential of embryonic VP derived from vascular disease-affected fibroblast-hiPSC, we generated several conventional DhiPSC lines from type-1 diabetic donor skin fibroblasts using a modified version of a non-integrative 7-factor episomal reprogramming system [27-29] (**Fig. S2a**). Reversion of conventional DhiPSC with LIF-3i culture (that includes the tankyrase inhibitor XAV939), resulted in changes from flattened (**Fig. S2b**) to dome-shaped $SSEA4^+TRA\text{-}1\text{-}81^+$ N-DhiPSC colony morphologies (**Fig 2a, Fig. S2e**). To validate the effects of XAV939 inhibition of tankyrase-PARP activity in DhiPSC, we verified proteolytic inhibition of key proteins targeted by tankyrase PARylation, including AXIN1 (which synergizes with GSK3β inhibition to stabilize the activated **β-**catenin complex [20]), and tankyrase 1 (PARP-5a) and tankyrase 2 (PARP-5b) (which self-regulate their own proteolysis by auto-PARylation) [30]. Accordingly, chemical inhibition of their degradation resulted in high accumulated levels of tankyrases 1/2 and AXIN1 in LIF-3i-reverted N-DhiPSC (**Fig. 2b**). These biochemical transitions were accompanied by naïve ESC-specific activation of phosphorylated STAT3 signaling and TFAP2C [31] expression, and increased protein expressions of a panoply of naïve-specific pluripotency factors (*e.g.*, NANOG, KLF2, NR5A2, TFCP2L1, STELLA/DPPA3, and E-CADHERIN; **Fig 2a-d**). Importantly, all N-DhiPSC lines possessed normal karyotypes (**Table S2, Fig. S2e**), and generated robust tri-lineage teratomas with significantly higher differentiation performances of organoid structures representing all three germ layers, in similar efficiencies to non-diabetic hiPSC (**Fig. 2e, S2f**).

LIF-3i reversion improved the efficiency of vascular lineage differentiation of diabetic donor-derived conventional hiPSC lines, and diminished the interline variability of VP

generation between independent hiPSC lines. We previously identified a FACS-purified $CD31^+CD146^+CXCR4^+$ embryonic VP population differentiated from conventional hiPSC that possessed both endothelial and pericytic functionalities [7]. Ischemia-damaged retinal vasculature was repaired by transplantation of hiPSC-derived $CD31^+CD146^+$ embryonic VP generated from conventional hiPSC that possessed prolific endothelial-pericytic differentiation potential and engrafted and rescued degenerated retinal vasculature following ischemia-reperfusion (I/R) injury.

Employing a modified version of our vascular differentiation protocol [7] (APEL system, **Fig. 3a**) [32,33], we observed that $CD31^+CD146^+$ VP cells were more efficiently generated, and with more rapid differentiation kinetics from both non-diabetic N-hiPSC and N-DhiPSC relative to their isogenic primed, conventional hiPSC counterparts (**Fig. 3b,c; Fig. S3a,b**). Kinetic analyses of parallel vascular differentiation cultures of N-hiPSC vs primed isogenic hiPSC revealed higher expression levels of vascular lineage transcripts (*e.g.*, *TIE1*, *TIE2*), higher expressions of vascular surface markers (*e.g.*, CD34, CD31, CD146, CD144), and a more rapid decrease of pluripotency markers (*e.g.,* SSEA4, TRA-1-81). Interestingly, the improved differentiation performance of N-hiPSC erased the poor efficiency and interline variability of vascular cell differentiation routinely observed between independent conventional fibroblast-derived hiPSC lines [7,12,34,35] . LIF-3i reversion permitted comparable efficiencies of generation of $CD31^+CD146^+CXCR4^+$ VP populations *regardless of conventional hiPSC donor source.* For example, fibroblast-derived N-DhiPSC and cord blood (CB)-derived N-CB-hiPSC lines generated similar efficiencies of VP, despite a higher VP differentiation efficiency of conventional CB-hiPSC [7] (**Fig. 3d, Fig. S3d**). Following MACS enrichment, $CD31^+CD146^+$ naïve and primed VP populations initially displayed similar and equalized expressions of a broad array of vascular markers (*e.g.*, CD31, CD34, CD144 and CD146) (**Fig. S3c**). Endothelial progenitor-specific ($CD31^+CD105^{hi}CD144^+$), pericytic ($CD31^+CD90^+CD146^+$) populations [36], and subcellular endothelial-specific organelles (*e.g.,* Weibel-Palade (WP) bodies, and coated pits; **Fig. 3e**) were also similarly generated in purified VP from either primed and naïve DhiPSC, or between naïve VP from alternate N-hiPSC origins (**Fig. S3d**); albeit with some minor differences (*e.g.*, more abundant transcytotic endothelial channels (TEC), and higher expressions of CD44 in naïve VP (**Figs. 3e, S3c**).

VP differentiated from N-DhiPSC possessed improved vascular functionality, lower culture senescence, and reduced sensitivity to DNA damage. Endothelium dysfunction in diabetics is characterized by poor endothelial cell survival, function, and DNA damage response (DDR). Although regenerative replacement of diseased vasculature requires high functioning cell therapies, previous studies of vascular differentiation with conventional fibroblast-hiPSC revealed poor and variable growth and expansion of vascular lineage cells, with high rates of apoptosis and early senescence [34,35]. To evaluate endothelial functionality of naïve $CD31^{+}CD146^{+}$ VP, purified VP populations were re-cultured and expanded in endothelial growth medium (EGM2). N-DhiPSC-derived VP were compared to isogenic primed-DhiPSC-derived VP for CD31 transcript expression (**Fig. 4a**), *in vitro* and *in vivo* NOD/Shi-*scid*/IL-2Rγ^{null} (NOG). Matrigel vascular tube formation assays (**Figs. 4, S4a,b**). endothelial acetylated-DiI-LDL (Ac-DiI-Ac-LDL) uptake assays (**Fig. 4c,d**), ethynyldeoxyuridone (EdU) cell cycle assays (**Figs. 4e, S4c**), and culture senescence assays (**Figs. 4f, S4d**). These studies collectively revealed that $CD31^{+}CD146^{+}$-enriched naïve VP maintained higher endothelial Ac-DiI-Ac-LDL uptake function, more enhanced proliferation, and significantly less culture senescence following re-culture and expansion.

To further evaluate the relative resistance of naïve VP to senescence, we probed genomic integrity maintenance by assaying for sensitivity to double stranded DNA breaks (DSBs) following treatment with the radiation damage mimetic neocarzinostatin (NCS), which triggers both DDR and pH2AX-mediated reactive oxygen species (ROS) signals [37]. Expression of phosphorylated p53 protein (P-p53), pH2AX, RAD51, RAD54, DNA-PK, which are all normally activated briefly following DDR and mediate repair of DSBs, were compared in re-cultured and expanded primed vs naïve VP, before and after treatment with NCS (**Fig. 5a-c, Fig. S5**). These studies revealed that levels of the DDR and DSB protein network (*e.g.*, phosphorylated H2AX, phosphorylated p53, RAD51, RAD54, phosphorylated DNA-PK) were all globally reduced in their expressions in both undifferentiated N-DhiPSC (**Fig. S5a**), as well as differentiated naïve normal VP and naïve diabetic VP (**Fig. 5a-c; Fig. S5b**), both before *and* following NCS DNA damage exposure. Collectively, these data demonstrated that naïve VP may mediate a reduced sensitivity to stress-induced DNA damage than do primed diabetic VP. These studies further suggested an improved genomic integrity of naïve VP *relative to VP generated from conventional counterparts* of both normal hiPSC and diseased DhiPSC.

Naïve diabetic VP injected into the vitreous of eyes with ischemia-damaged retina survived and engrafted into retinal vasculature with high efficiency. To evaluate the potential of naïve VP for *in vivo* engraftment and repair of ischemic retinal vessels, we employed a previously described immune-deficient murine model of ocular I/R injury (**Fig. S6a**) [7]. The sequential loss of murine host retinal vasculature endothelial cells (ECs) following ocular I/R injury was detected with an antibody specific to mouse anti-CD31, and the vascular basement membrane was detected with a murine anti-collagen type-IV antibody. In this model, ischemic damage is more severe in capillaries and veins presumably due to their higher collapsible nature under increased intraocular pressure compared to arteries. This approach is feasible because despite ischemic damage to acellular capillaries, the basement membrane shared by EC and pericytes in retinal capillaries remains intact.

$CD31^+CD146^+$-sorted human VP cells were differentiated from isogenic primed vs N-DhiPSC as above, cultured briefly in EGM2, and 50,000 VP cells were injected directly into the vitreous body of NOG recipient eyes 2 days following I/R injury. Human cell viability and engraftment in murine retina was evaluated at 1, 2, 3, and 4 weeks following human VP injections with human-specific anti-human nuclear antigen (HNA) antibody staining. One week following vitreous body injection in I/R-damaged eyes, HNA^+ naive VP were observed to survive in significantly greater frequencies than primed VP in the superficial layer of the retina (**Fig. 6a, S6b**). Additionally, HNA^+ naive VP assumed adherent abluminal pericytic and luminal endothelial positions with greater frequency (**Fig. 6b, Fig. S6c),** and appeared to favor venous engraftment of blood vessels with large diameter than arteries suggesting a preferential migration in response to injury signals [7]. In contrast, and as previously demonstrated for non-diabetic fibroblast-derived hiPSC, primed DhiPSC-derived VP cells survived poorly and migrated inefficiently into ischemia-damaged blood vessels, and instead remained in either the vitreous, or adherent to the adjacent superficial layer of the retina (**Fig. 6a, b**). Naïve diabetic VP not only survived 1-4 weeks post injection robustly in the superficial retinal ganglion cell layers (GCL), but also engrafted into murine retinal vessels with significantly greater efficiencies than VP differentiated from conventional, primed DhiPSC (**Fig. 6c,d; S6c**).

Interestingly, immunostaining with anti-human CD34 and anti-human CD31 antibodies confirmed significant HNA^+ naïve VP engraftment in the intima of murine host ischemia-damaged capillaries located in the deep neural retinal layers (**Fig. 7**). At 2 weeks following I/R injury, HNA^+, human $CD34^+$, and human $CD31^+$ vessels were readily detected in naïve-VP-injected retinae at significantly higher rates than primed VP-injected retinae. Notably, naïve VP had migrated from the deep vascular layers of the GCL, and migrated all the way to the inner nuclear layer (INL) of the murine neural retina (*e.g.*, ~20 engrafted human vessels per 450μm cross section areas; **Fig. 7d-g**). In contrast, injected primed VP remained primarily in the superficial vascular layer of the retinal GCL without further migration. These data also demonstrated that chimeric human-murine capillaries were detected not only in linear and branch point vascular segments, but also migrated more efficiently from vitreous to the deep vascular neural retinal layers; suggesting that an efficient reparative injury-induced vasculogenesis had occurred following naïve VP (but not primed VP) cellular therapy.

N-hiPSC tightly regulated 'leaky' lineage-primed gene expression, and were configured with de-repressed, activation-poised bivalent histone marks at key developmental promoters. The murine naïve pluripotent state, which has higher differentiation potential than the primed murine pluripotent state [11], is distinguished by a chromatin that is poised for unbiased gene activation [38]; global reductions of CpG DNA methylation [39], and decreased repressive H3K27me3 histone deposition at bivalent Polycomb repressor Complex 2 (PRC2)-regulated promoter sites [40,41] . Accordingly, as was reported for normal fibroblast-N-hiPSC [12], all three fibroblast-N-DhiPSC lines exhibited significant reductions in global 5-methylcytosine (5MC)-associated CpG DNA methylation following LIF-3i reversion (**Fig S8a,b**). The detection of increased global levels for 5-hydroxymethylcytosine (5hMC) in N-hiPSC relative to primed DhiPSC further suggested a contribution of naïve-like TET-mediated active CpG demethylation [39].

To explore the molecular mechanisms that may drive improved functionality of LIF-3i-reverted N-hiPSC, we probed epigenetic configurations that regulate developmental gene expression. A simultaneous bioinformatics analyses of both microarray expression and Infinium CpG methylation arrays of lineage-specifying PRC2 gene targets (before and after

LIF-3i-reversion of a broad array of isogenic hiPSC lines), revealed a broad rewiring of the lineage-specifying machinery. CpG DNA hypomethylation at promoter sites of PRC2 genes were broadly hypomethylated in N-hiPSC lines relative to their primed counterparts with a significant decrease of expression in many lineage-specifying PRC2 targets (**Fig. 8a,b**). These studies revealed that in comparison to primed fibroblast-hiPSC, isogenic N-hiPSC displayed significantly less baseline epigenetic CpG methylation-regulated repression of lineage-specifying PRC2 genes, *despite* a *broad* silencing of lineage-primed transcriptional targets of PRC2 as previously reported [12] (**Figs. 8b, S8c, Table S3**).

A critical mechanism for protecting naïve mouse ESC from lineage priming is via regulating the poised silencing or activation of lineage-specifying genes via bivalent H3K27me3 repressive and H3K4 activation histone marks, and RNA Polymerase II (POLII) pausing at promoter sites [40-42]. Thus, we next assessed the protein abundance of PRC2 components which mediate repressive H3K27me3 deposition on bivalent promoters in naïve versus primed normal and DhiPSCs (**Fig. 8c**). Interestingly, these studies revealed significantly *decreased* abundance of multiple components of the PRC2 complex, including the enzymatic subunits EZH1, EZH2, and the cofactor subunit JARID2 [43] (which drives the localized recruitment of PRC2 at developmental promoters in mouse ESC). To functionally validate the activity of PRC2 targets, we employed chromatin immunoprecipitation followed by qPCR (ChIP-PCR) on previously characterized lineage-specific bivalent gene promoters (*e.g.*, *PAX6, MSX2, GATA6, SOX1, HAND1, GATA2;* (**Fig. 8d, S8d, Table S3**) to investigate the levels of bivalent active (H3K4me3) and repressive (H3K27me3) histone marks at these key lineage-specifying promoters. These studies revealed significant H3K27me3 reductions (5-15% from isogenic primed E1C1 and E1CA1 DhiPSC lines) following LIF-3i reversion.

Collectively, these CpG DNA methylation and histone mark studies revealed a relatively de-repressed naive epigenetic state in N-hiPSC that appeared more poised for activation than primed DhiPSC; with a potentially decreased barrier for multi-lineage gene activation relative to primed DhiPSC. Thus, as was previously demonstrated for naïve murine ESC [38,40], despite a tighter regulation of 'leaky' lineage-primed gene expression that was presumptively silenced through alternate naïve-like epigenetic mechanisms of bivalent promoter repression (*e.g.*, promoter site RNA POLII pausing [40]), N-hiPSC appeared poised with a lower epigenetic barrier for unbiased multi-lineage differentiation.

Differentiated naïve VP possessed vascular lineage epigenetic and transcriptional de-repression and reduced non-vascular lineage-primed gene expression. To determine the downstream impact of an epigenetic state with an apparently lower barrier for vascular lineage activation, we investigated the epigenetic configurations of vascular-lineage specific gene promoters in differentiated VP by ChiP-PCR. We selected the promoters of downstream genes regulated by the PRC2-regulated factor GATA2, which promotes expression of genes of endothelial-specific identity and function (*e.g.*, *CD31*, *vWF*, *endothelin-1*, and *ICAM2*) [10]. We also selected promoters of genes known to be activated by chemical EZH2 and histone deacetylases (HDAC) de-repression in human endothelial progenitor cells (EPC) (*e.g.*, *CXCR4*, *DLL1*, and *FZD7*) [44].

$CD31^{+}CD146^{+}$ VPs derived from either primed vs naïve DhiPSCs were MACS-purified, briefly expanded in EGM2, and ChIP-PCR was performed on promoter sites of these genes. Strikingly, relative to primed VP, naïve VP displayed significantly increased marks for epigenetic activation (H3K4me3), with simultaneously reduced marks of promoter repression (H3K27me3) (**Fig. 8e**) for genes determining vascular functionality (*e.g., CD31*, *vWF*, *endothelin-1*, *ICAM2*, and *CXCR4*). Importantly, repressive H3K27me3 marks on naïve VP were increased relative to primed VP for the non-vascular lineage muscle-specific promoter MYOD1. qRT-PCR expression analysis of these transcripts confirmed that naïve VP indeed expressed significantly higher levels of these vascular genes and lower levels of non-vascular genes (*e.g., PAX6, MSX2, MYOD1*) (**Fig. 8f**). These data were consistent with an improved epigenetic state in N-DhiPSC that potentiated a lower transcriptional barrier for generating VP with higher vascular-specific gene expressions, decreased non-vascular lineage-primed gene expressions, and ultimately greater *in vivo* functionality.

DISCUSSION

These studies describe for the first time the advantage of employing an alternative tankyrase inhibitor-regulated human naïve pluripotent state for improving vascular regenerative therapies. We have shown that VP differentiated from naïve patient-specific hiPSC maintained greater genomic stability than VP generated from conventional hiPSC, and had higher expression of vascular identity markers, decreased non-lineage gene expression, and

were superior in migrating to and re-vascularizing the deep neural layers of the ischemic retina. More broadly, naïve tankyrase inhibitor-regulated hiPSC represent a new class of human stem cells for regenerative medicine with improved multi-lineage functionality. In contrast, conventional hiPSC cultures adopt transcriptomic, epigenetic, and signaling signatures of lineage-primed pluripotency, and display a heterogeneous propensity for lineage bias and differentiation. To date, there has not been a human naïve pluripotent stem cell method demonstrating effectiveness for pre-clinical cellular therapies.

In these studies, diabetic naïve VP with angioblast-like endothelial-pericytic potential possessed improved vascular potency and functionality *in vivo* for re-vascularizing the ischemic retina. These transplantable naïve VP can be generated in unlimited quantities and injected at multiple target sites in multiple treatments and time periods. Such epigenetically plastic VP are non-existent in circulating adult peripheral blood or bone marrow. For example, adult EPC are limited in multipotency, expansion, homing, and functionality in diabetes [2,14-16]. The generation of embryonic VP differentiated from a diabetic patient's N-hiPSC bypasses this obstacle. Diabetic N-hiPSC are more effectively reprogrammed from a donor's skin or blood cells back to a pre-diseased state, and subsequently differentiated to unlimited quantities of pristine transplantable VP; which unlike adult diabetic EPC would be unaffected by the functional and epigenetic damage caused by chronic hyperglycemia.

Our previous studies demonstrated that embryonic VP derived from conventional CB-derived hiPSC generated with higher and more complete reprogramming efficiencies had decreased lineage-primed gene expression and displayed limited but long-term regeneration of degenerated retinal vessels [7]. In comparison, conventional skin fibroblast-derived hiPSC lines with higher rates of reprogramming errors and lineage-primed gene expression displayed poorer vascular differentiation and *in vivo* retinal engraftment efficiencies relative to conventional CB-hiPSC. Here, this obstacle was solved by demonstrating that patient-specific $CD31^{+}CD146^{+}$ endothelial-pericytic VP differentiated from diabetic skin fibroblast donor-derived hiPSC were more efficiently generated from N-hiPSC than from conventional fibroblast hiPSC, and with higher epigenomic stability, reduced lineage priming, and improved *in vivo* engraftment capacity in ischemia-damaged blood vessels. Multiple cell types (*e.g.*, vascular endothelium, pericytes, retinal neurons, glia, and retinal pigmented epithelium) could all potentially be differentiated from the same autologous or HLA-

compatible, banked patient-specific hiPSC line for a comprehensive repair of ischemic vascular and macular degenerative disease.

The studies herein have also demonstrated that the obstacle of incomplete reprogramming and lineage priming of conventional fibroblast-hiPSC can be overcome with molecular reversion to a tankyrase inhibitor-regulated naïve epiblast-like state with a more primitive, unbiased epigenetic configuration. N-DhiPSC possessed a naïve epiblast-like state with decreased epigenetic barriers for vascular lineage specification, and decreased non-vascular lineage specific gene expression. Interestingly, compared to conventional lineage primed DhiPSC, tankyrase-inhibited N-DhiPSC possessed a de-repressed naïve epiblast-like epigenetic configuration at bivalent developmental promoters that was highly poised for non-biased, multi-lineage lineage specification, and was configured in a manner akin to naïve murine ESC [38-41].

Zimmerlin *et al* first reported that continuous culture of conventional hiPSC with 2i (GSK3β/MEK inhibitors CHIR99021 and PD0325901) plus only the tankyrase/PARP inhibitor XAV939 (LIF-3i) was sufficient for reversion of conventional hPSC to a naïve-like pluripotent state with significantly enhanced developmental potency to all three embryonic germ layer lineages [12]. Interestingly, several recent studies also incorporated tankyrase/PARP inhibition into their small molecule cocktails to significantly improve the functionality of either murine PSC [19], or alternatively human PSC [21, 45] with a non-naive epiblast-like epigenetic phenotype. For example, the LCDM [45] and mouse expanded potential stem cell (EPSC) [19,21] approaches incorporated either tankyrase or PARP inhibiters in their chemical cocktails to improve both trophectoderm and embryonic contribution of mESC into murine chimeras. Both systems utilized tankyrase/PARP inhibition either at the initiation [45] or throughout [19,21] PSC expansion. Remarkably, tankyrase/PARP inhibition of mESC and hPSC preserved the capacity of cleavage-stage murine blastomeres for trophectoderm/ICM lineage segregation. Supplementation with XAV939 to other human naïve-like pluripotent states prior to directed differentiation also led to a significant reduction of lineage-primed gene expressions, and partially rescued a multi-lineage differentiation block [46]. Unlike the original LIF-3i method, subsequent tankyrase-inhibited human PSC methods did not continuously incorporate a MEK inhibitor in their initial growth conditions, which may be necessary to epigenetically

potentiate and maintain a naïve epiblast-like pluripotent state [38,40]. LIF-3i was sufficient for bulk, stable reversion and expansion of a large repertoire of conventional lineage-primed hiPSC to a human naïve pluripotent state that possessed characteristics of human preimplantation ICM and mESC, including high clonal proliferation (*i.e.*, without requirement of apoptosis inhibition; Rock/Rho kinase inhibitor), MEK-ERK/bFGF signaling independence, activated JAK/STAT3 phosphorylation/signaling, expression of human preimplantation epiblast-like core pluripotency circuits, distal OCT4 enhancer usage, global DNA CpG hypomethylation, and increased expressions of activated β-catenin. Moreover, tankyrase inhibitor-based naïve reversion produced N-hiPSC that retained normal patterns of genomic CpG methylated imprints, reduced lineage-primed gene expression, improved multi-lineage differentiation potency, and did not require reversion culture back to primed conditions prior to differentiation.

The mechanism by which XAV939 stabilized and expanded the functional pluripotency of an inherently unstable human naïve state in classical 2i conditions currently remains incompletely defined. As previously described [12], the LIF-3i trio chemical cocktail minimally employs MEK inhibition (PD0325901) to block lineage-primed differentiation, along with a simultaneous and parallel dual synergy of XAV939 with the GSK3β (CHIR99021) inhibitor to augment WNT signalling [20] . The presumptive mechanism of augmented WNT signalling is via inhibition of tankyrase-mediated degradation of AXIN, which causes stabilization and increased cytoplasmic retention of the activated isoform of β-catenin (which decreases β-catenin-TCF interactions). However, in humans, the repertoire of proteins directly targeted by tankyrase post-translational PARylation extends far beyond WNT signalling, and includes proteins (*e.g.*, AXIN1 and 2, APC2, NKD1, NKD2, and HectD1) with diverse biological functions that potentially cooperate to support a stable pluripotent state [47]. These functions include regulation of telomere elongation and cohesion (TRF1), YAP signalling (angiomotin), mitotic spindle integrity (NuMa), GLUT4 vesicle trafficking (IRAP), DNA damage response regulation (CHEK2), and microRNA processing (DICER). Interestingly, TRF1 was identified as an essential factor for iPSC reprogramming in mouse and human PSC [48]. Additionally, although LIF-3i includes MEK inhibition and promotes global and genome-wide low DNA methylation, and, it does not appear to impair genomic CpG methylation at imprinted loci [12]. Although the mechanism of such imprint preservation by XAV939 in the context of MEK

inhibitor is currently obscure, PARylation has been shown to safeguard the Dnmt1 promoter in mouse cells, and antagonizes aberrant hypomethylation at CpG islands, including at imprinted genes [49,50]. Thus, the role of PARylation on DNA methylation requires deeper investigation.

Diabetic hyperglycemic alterations of blood vessel viability and integrity lead to multi-organ dysfunction that results in endothelial dysfunction linked to epigenetic remodeling [17] (*e.g.*, DNA methylation [51], histone marks [52,53] and oxidative stress [54,55]). Several studies have shown that these aberrant epigenetic changes may be partially overcome by genome-wide chemical treatments that restore some endothelial function [56,57]. The extent of retention of diseased 'diabetic epigenetic memory' at developmental genes from incomplete or ineffective reprogramming within DhiPSC-derived lineages and its role in impaired regenerative capacity remains unclear, and marked by high variability in differentiation efficiency or retention of diseased phenotype [58-61]. For example, endothelial differentiation of iPSC generated from diabetic mice displayed vascular dysfunction, impaired *in vivo* regenerative capacity, and diabetic iPSC displayed poor teratoma formation [63] . Human iPSC from patients with rare forms of diabetes-related metabolic disorders have similarly shown significant functional endothelial impairment [58]. Transient chemical demethylation of T1D-hiPSC was sufficient to restore differentiation in resistant cell lines and achieve functional differentiation into insulin-producing cells [18].

In summary, these studies, we produced highly functional VP cells from N-hPSC, independent of their genetic background or diseased diabetic origin. Naïve reversion of conventional D-hiPSC potentiated a further epigenetic remodeling of reprogrammed diabetic fibroblasts that avoided differentiation into dysregulated in dysfunctional endothelial cells with 'diabetic epigenetic memory'. Similarly, tankyrase inhibitor-regulated N-hiPSC are expected to improve the poor and variable hiPSC differentiation generation of other disease-affected tissues affected in diabetes [64] including pancreatic, renal, hematopoietic, retinal, and cardiac lineages. The further optimization of tankyrase-inhibited human primed and naïve pluripotent stem cells in defined, clinical-grade conditions will significantly advance the efficacy of hiPSC-based regenerative approaches.

METHODS

Bioethics. hESC lines used in these studies as controls for hiPSC were obtained commercially from the Wisconsin International Stem Cell Bank (WISCB). All hESC experiments proposed conform to guidelines outlined by the National Academy of Sciences, and the International Society of Stem Cell Research (ISSCR) Commercially-acquired hESC are under purview of the Johns Hopkins University (JHU) Institutional Stem Cell Research Oversight (ISCRO), and conform to Institutional standards regarding informed consent and provenance evaluation. All experiments proposed received approval by the JHU ISCRO committee. All animal use and surgical procedures were performed in accordance with protocols approved by the Johns Hopkins School of Medicine Institute of Animal Care and Use Committee (IACUC) and the Association for Research of Vision and Ophthalmology statement for the Use of Animals in Ophthalmic and Visual Research.

Conventional and LIF-3i naïve reversion cultures of hESC and hiPSC. All human embryonic stem cells (hESC) and hiPSC lines in these studies were maintained and expanded in undifferentiated conventional feeder-free primed states in Essential 8 (E8) medium, or naive-reverted with the LIF-3i system as described [12,13].

Conventional cultures of hiPSC were propagated using commercial E8 medium (ThermoFisher Scientific), or an in-house variant formulation consisting of DMEM/F-12 supplemented with 2.5mM L-Glutamine, 15mM HEPES and 14mM sodium bicarbonate (ThermoFisher Scientific, cat# 11330), 50-100ng/mL recombinant human FGF-basic (Peprotech), 2ng/mL recombinant human TGF-β1 (Peprotech), 64μg/mL L-ascorbic acid-2-phosphate magnesium (Sigma), 14ng/mL sodium selenite (Sigma), 10.7 μg/mL recombinant human transferrin (Sigma), and 20μg/mL recombinant human insulin (Peprotech). Conventional hiPSC were expanded in E8 onto Vitronectin XF (STEMCELL Technologies) matrix-coated tissue culture-treated 6-well plates (Corning). E8 medium was replaced daily and hiPSC were gently passaged every 5-6 days by mechanical selection or bulk passaged using non-enzymatic reagents (i.e., Versene solution (ThermoFisher Scientific) or Phosphate-Buffer-Saline (PBS)-based enzyme-free cell dissociation buffer (ThermoFisher Scientific, #13151).

LIF-3i medium was prepared fresh every other week and consists of DMEM/F-12 supplemented with 20% KnockOut Serum Replacement (KOSR, ThermoFisher Scientific), 0.1mM MEM non-essential amino acids (MEM NEAA, ThermoFisher Scientific), 1mM L-Glutamine (ThermoFisher Scientific), 0.1mM β-mercaptoethanol (Sigma), 20ng/mL recombinant human LIF (Peprotech), 3μM CHIR99021 (Tocris or Peprotech), 1μM PD0325901 (Sigma or Peprotech), and 4μM XAV939 (Sigma or Peprotech). Prior to switching between E8 and LIF-3i media, hPSC were adapted for one passage in LIF-5i, as described [12,13]. LIF-5i was prepared by supplementing LIF-3i with 10μM Forskolin (Stemgent or Peprotech), 2μM purmorphamine (Stemgent or Peprotech) and 10ng/mL recombinant human FGF-basic (Peprotech). Briefly, primed hiPSC were adapted overnight by substituting E8 with LIF-5i medium. The next day, hiPSC were enzymatically dissociated (Accutase, ThermoFisher Scientific) and transferred onto irradiated mouse embryonic fibroblast (MEF) feeders in LIF-5i medium for 2 to 3 days. All subsequent passages were grown into LIF-3i medium onto MEF feeders. Isogenic E8 cultures were maintained in parallel for simultaneous phenotypic characterization, as described in detail [12,13].

Primed *vs.* naive hiPSC teratoma assays. For teratoma assays, isogenic primed and LIF-3i hiPSC cultures were maintained in parallel for 9 passages. Teratomas were directly generated from a fixed number of cells ($5x10^6$) and duration (8 weeks) in isogenic primed *vs*. LIF-3i hiPSC conditions. LIF-3i hiPSC colonies did not require chemical manipulation or re-priming culture steps prior to enzymatic harvest from culture and direct injection into NOG mice. Adherent hiPSC were collected using Accutase and counted using Countess counter (ThermoFisher Scientific). For all experiments, $5x10^6$ hiPSC were admixed with Growth factor reduced Matrigel (Corning, cat# 356230) on ice. Cells were injected subcutaneously into the hind limbs of immunodeficient NOG male sibling mice. Teratomas were dissected 8 weeks following injection and fixed by overnight immersion in PBS, 4% formaldehyde. All tissues were paraffin-embedded, and microsectioned (5μm thickness) onto microscope glass slides (Cardinal Health) by the Histology laboratory from the Pathology Department at the Johns Hopkins University. To account for heterogeneous teratoma histological distribution, 15 individual equally-spaced sections were immunostained per tissue for each antigen of interest and quantification. Slides were heated in a hybridization oven (ThermoFisher

Scientific) at 60°C for 20 minutes and then kept at room temperature for 1 hour to dry. Paraffin was eliminated by three consecutive immersions in xylenes (Sigma) and sections were rehydrated by transitioning the slides in successive 100%, 95%, 70% and 0% ethanol baths. Sections were placed in 1X wash buffer (Dako) prior to heat-induced antigen retrieval using 1X Tris-EDTA, pH9 target retrieval solution (Dako) and wet autoclave (125°C, 20 min). Slides were cooled and progressively transitioned to PBS. After 2 washes, tissues were blocked for 1 hour at room temperature using PBS, 5% goat serum (Sigma), 0.05% Tween 20. Endogenous biotin receptors and streptavidin binding sites were saturated using the Streptavidin/Biotin Blocking kit (Vector Laboratories). All antibodies were diluted in blocking solution. Sections were incubated overnight at 4°C with monoclonal mouse anti-NG2 (Sigma, C8035, 1:100), mouse anti-SOX2 (ThermoFisher Scientific, MAS-15734, 1:100) or rabbit anti-cytokeratin 8 (Abcam, ab53280, 1:400) primary antibodies, washed 3 times, incubated for 1 hour at room temperature with biotinylated goat anti-mouse or goat anti-rabbit IgG antibodies (Dako, 1:500), washed 3 times and incubated with streptavidin Cy3 (Sigma, 1:500) for 30 minutes at room temperature. After 2 washes, tissues were incubated for 2 hours at room temperature with a second primary antibody (i.e., anti-Ki67) differing in species from the first primary antibody. After incubation with rabbit (Abcam, ab16667, 1:50) or mouse (Dako, M7240, 1:50) anti-Ki67 monoclonal antibody, sections were washed 3 times and incubated for 1 hour at room temperature with highly cross-adsorbed Alexa Fluor 488-conjugated goat anti-rabbit or goat anti-mouse secondary antibody (ThermoFisher Scientific, 1:250). Sections were washed twice, incubated with 10µg/mL DAPI (ThermoFisher Scientific, D1306) in PBS, washed 3 times in PBS and slides were mounted with coverslips using Prolong Gold Anti-fade reagent (ThermoFisher Scientific) for imaging. Isotype controls for mouse (ThermoFisher Scientific) and rabbit (Dako) antibodies were substituted at matching concentration with primary antibodies as negative controls.

For teratoma organoid quantifications, photomicrographs were obtained using a 20X objective and Zeiss LSM 510 Meta Confocal Microscope. Image processing and quantification was performed using NIS-Elements software (Nikon). The ROI editor component was applied to autodetect regions of interest in the Cy3 channel that delineated lineage-defined structures (i.e., Cytokeratin 8^+ definitive endoderm, $NG2^+$ chondroblasts, $SOX2^+$ neural rosettes) within teratomas. Thresholding and restrictions were standardized in

the Object Count component and applied to detect and export the number of $DAPI^+$ and $Ki67^+$ nuclei within ROIs for all analyzed sections.

Reprogramming of diabetic fibroblasts to conventional hiPSC. Adult human Type-I diabetic (T1D) fibroblasts were purchased from DV Biologics, and cultured in fibroblast culture medium (I-Gro medium, DV Biologics). For reprogramming, single cells were obtained using Accutase and counted. Episomal expression of seven genes (*SOX2*, *OCT4*, *KLF4*, *c-MYC*, *NANOG*, *LIN28*, *SV40LT*) was accomplished by nucleofection of $1x10^6$ diabetic fibroblast cells with 2 μg each of three plasmids, pCEP4-EO2S-EN2L, pCEP4-EO2S-ET2K, and pCEP4-EO2S-EM2K as described [27,28]. Fibroblasts were nucleofected using human dermal fibroblast nucleofector kits (Lonza, VPD-1001) with Amaxa nucleofector program U-023. Nucleofected cells were transferred onto irradiated MEF in fibroblast growth medium supplemented with 10 μM Rho-associated, coiled-coil containing protein kinase (ROCK) inhibitor Y27362 (Stemgent). The next day, 2 mL of DMEM/F-12 supplemented with 20% KOSR, 0.1mM MEM NEAA, 1mM L-Glutamine, 0.1mM β-mercaptoethanol, 50 ng/mL bFGF, 10 μM Y27362, 5 μg/mL ascorbic acid, and 3 μM CHIR99021 was added. Half of the medium was replaced with fresh medium without Y27362 every other day, until hiPSC colonies appeared. Individual hiPSC colonies were manually isolated, further expanded onto vitronectin-coated plates in E8 medium, or cryopreserved.

Antibodies. Source and working dilutions of all antibodies used in these studies for Western blots, FACS, genomic dot blots, ChiP, and immunofluorescence experiments are listed in **Table S3.**

Western blotting. Cells were collected from either primed (E8 media on vitronectin-coated plates) or naïve (LIF-3i/MEF plates) conditions with Enzyme-Free Cell Dissociation Buffer (Gibco, 13151-014). Cells were washed in PBS and pelleted. Cell pellets were lysed in 1x RIPA buffer (ThermoFisher Scientific, 89900), 1mM EDTA, 1x Protease Inhibitor (ThermoFisher Scientific, 78430), and quantified using the Pierce bicinchoninic acid (BCA) assay method (ThermoFisher Scientific). 25μg of protein per sample was loaded on a 4-12% NuPage Gel (ThermoFisher Scientific, NP0336) according to manufacturer's recommendations. The gel was transferred using the iBlot2 (Life Technologies), blocked in

Tris-buffered saline (TBS), 5% non-fat dry milk (Labscientific), 0.1% Tween-20 (TBS-T) for 1 hour, and incubated overnight at 4°C in with anti-phosphorylated-STAT3 primary antibody (Cell Signaling, 9145) according to manufacturer's protocols. Membranes were rinsed 3 times in TBS-T, incubated with horseradish peroxidase (HRP) –linked goat anti-rabbit secondary antibody (Cell Signaling, 7074) for 1 hour at room temperature, rinsed 3 times, and developed using Pierce ECL Substrate (ThermoFisher Scientific, 32106). Chemiluminescence detection was imaged using an Amersham Imager 600 (Amersham). Anti-actin antibody staining was performed for each membrane as a loading control.

Directed neuroectodermal, endodermal, and vascular differentiations of primed *vs.* naïve hiPSC. To examine the differentiation competence of N-hiPSC, we directly differentiated LIF-3i-reverted vs their primed isogenic hiPSC counterparts in parallel, as described [12,13]. To minimize assay variations within directed differentiation experiments, paired primed and LIF-3i isogenic hiPSC lines were simultaneously cultured into defined, feeder-free differentiation systems. This approach was previously detailed for functional comparison of primed vs naïve hiPSC states [12,13]. Detailed information for the origins and derivation of the hiPSC lines used for these assays was previously reported [12]. Differentiation to neural progenitors was performed using GIBCO PSC neural induction medium (NIM; ThermoFisher Scientific, A1647801) and the manufacturer's recommendations. Differentiation into definitive endodermal progenitors was achieved using the StemDiff Definitive Endoderm Kit (StemCell Technologies) following manufacturer's protocols.

Vascular differentiation of VP from primed and naïve hiPSC is modified and optimized from methods previously described [7], and is summarized in **FIG. 3A**. VP differentiation was performed using a modified protocol based on the STEMdiff APEL-Li medium system (**Fig. 3a**) [32]. Briefly, APEL-2Li medium (StemCell Technologies, #5271) was supplemented with Activin A (25 ng/mL), VEGF (50 ng/mL), BMP4 (30 ng/mL), and CHIR99021 (1.5 μM) for the first 2 days and then APEL-Li including VEGF (50 ng/mL) and SB431542 (10μM) until analyzed; medium was replaced every 2 days until cells were harvested.

Flow cytometry analysis of vascular differentiations and FACS purification of $CD31^{+}CD146^{+}$ endothelial-pericytic embryonic VP populations. Recipes for all

differentiation reagents, antibodies, and PCR primers were previously provided in detailed published Supplementary Tables [7]. For flow cytometry analysis of vascular differentiations, cells were washed once in PBS, and enzymatically digested with 0.05% trypsin-EDTA (5 min, 37°C), neutralized with FCS, and cell suspensions were filtered through a 40 μm cell-strainer (Fisher Scientific, Pittsburgh, PA). Cells were centrifuged (200 g, 5 min, room temperature) and re-suspended in staining buffer (EBM alone or 1:1 EMG2:PBS). Single cell suspensions ($<1x10^6$ cells in 100 μL per tube) were incubated for 20 min on ice with directly conjugated mouse monoclonal anti-human antibodies and isotype controls. Cells were washed with 3 mL of PBS, centrifuged (300g, 5 min, room temperature), and resuspended in 300 μL of staining buffer prior to acquisition. Viable cells were analyzed (10,000 events acquired for each sample) using the BD CellQuest Pro analytical software and FACSCalibur™ flow cytometer (BD Biosciences). All data files were analyzed using Flowjo analysis software (Tree Star Inc., Ashland, OR).

FACS of primed *vs.* naive VP populations was performed at the Johns Hopkins FACS Core Facility with a FACS Aria III instrument (BD Biosciences, San Jose, CA). Cell suspensions from APEL vascular differentiations were incubated with mouse anti-human CD31-APC (eBioscience, San Diego, CA) and CD146-PE (BD Biosciences) antibodies for 30 min on ice, and FACS-purified for high CD31 and CD146 expression, plated onto fibronectin-coated plates in EGM2, and expanded to 80-90% confluency for 7-9 days prior to in vitro analyses or *in vivo* injections into the eyes of I/R-treated NOG mice.

Vascular functional assays. The methods for Dil-acetylated-LDL uptake assays, Matrigel tube and Matrigel plug assays, EdU proliferation assays, β-galactosidase senescent assays were all described previously [7], and are summarized below briefly.

For Dil-Acetylated-Low Density Lipoprotein (Dil-Ac-LDL) uptake assays**,** FACS-purified $CD31^+CD146^+$ primed vs naïve VP populations were expanded in EGM2 medium ~7 days to 60 to 70% confluency on fibronectin pre-coated 6-well plates (1-1.5 x 10^5 cells/well) prior to Dil-Ac-LDL uptake assays (Life Technologies, Cat No. L-3484). Fresh EGM2 medium supplemented with 10 μg/mL Dil-Ac-LDL, was switched before assays, and incubated for 4 hours at 37°C. Cells were washed in PBS and Dil-Ac-LDL-positive cells imaged with a Nikon

Eclipse Ti-u inverted microscope (Nikon Instruments Inc., Melville, NY) and Eclipse imaging software. Cells were also harvested with Accutase (5 min, 37°C) and Dil-Ac-LDL$^+$ cells quantitated by flow cytometry.

In vitro vascular functionality of primed vs naïve VP was determined with Matrigel vascular tube-forming assays as previously described [7]. FACS-purified CD31$^+$CD146$^+$ VP were expanded in EGM2 on fibronectin-coated (10 μg/mL). tissue culture plates. Adherent cells were treated with Accutase for 5 min, and collected into single cell suspensions. VP cells were transferred in 48 well plates (2x10^5 cells/ well in EGM2 medium) pre-coated with Matrigel (Corning, #356237, 200 μL/well). The next day, phase contrast pictures of vascular tube formations were imaged with an inverted Eclipse Ti-u Nikon microscope (Nikon Instruments Inc., Melville, NY) and Eclipse imaging software. To confirm the vascular functionality of primed vs naive VP populations *in vivo*, FACS-purified CD31$^+$CD146$^+$ VP populations were expanded for 7-10 days in EGM2, harvested as above, resuspended in Matrigel (Corning, #356231), plugs, and injected subcutaneously into NOG mice. Capacity for three-dimensional human blood vessel formation was quantified two weeks later using human CD31 (DAKO) immuno-histochemistry of harvested Matrigel plugs, as described [7].

For senescence assays, naïve vs primed VP populations were plated onto fibronectin (10 μg/mL)-coated 6-well tissue culture plates, and VP were expanded in EGM2 for up to 30 days (3-6 passages), and senescent cells were assayed for acidic senescence-associated ß-galactosidase activity. Cells were grown to ~60-80% confluency in 12-well fibronectin-coated plates prior to analysis. Cells were fixed in 2% paraformaldehyde and β-galactosidase activity was quantified by detecting hydrolysis of the X-gal substrate by colorimetric assay as per manufacturer's protocol for detection of senescent cells. (Cell Signaling Technology, Danvers, MA). Nuclei were counterstained using the fluorescent dye Hoechst 33342 (BD Biosciences). Total number of Hoechst+ cells and blue X-Gal+ senescent cells were automatically enumerated using an inverted Eclipse Ti-u Nikon microscope and the Object Count component of the NIS Elements software. For each sample, 2 individual wells were photographed at five independent locations using a 20x objective. Results are presented as Mean ± SEM.

Transmission Electron Microscopy (TEM) of VP. Primed vs naïve VP were plated onto fibronectin (10 μg/mL) coated Labtek chambers, culture expanded in EGM2, and fixed for TEM as previously described at the Wilmer Microscopy Core [7]. Sections were imaged with a Hitachi H7600 TEM at 80KV (Gaithersburg, MD) and a side mount AMT CCD camera (Woburn, Mass).

NCS DNA damage response assays. Parallel isogenic primed and LIF-3i DhiPSC were simultaneously differentiated into VP using APEL medium, as described above. CD31+CD146+ VP cells were expanded in EGM2 (3 passages) onto fibronectin-coated (10μg/mL) 6-well plates (for Western blot analysis), or alternatively the last passage was transferred onto 8-well Nunc Labtek II chamber slides for immunostaining. To induce DNA damage, expanded VP cells were incubated for 5 hours in EGM2 supplemented with 100 ng/mL of the radiomimetic agent neocazinostatin (NCS, Sigma). Untreated VP cells were analyzed in parallel as control. Western blot analysis was performed as described above. For detection of phosphorylated H2AX by immunofluorescence, VP cells were fixed for 10 minutes using 1% paraformaldehyde in PBS. For immunofluorescent staining of chambered slides, fixed cells were blocked for non-specific staining and permeabilized using a blocking solution consisting of PBS, 5% goat serum (Sigma) and 0.05% Tween 20 (Sigma). Samples were incubated overnight at 4°C with a rabbit anti-human phospho-H2AX antibody (Cell Signaling, #9718) diluted (1:200) in blocking solution. The next day, VP cells were washed (Dako wash buffer, Dako) and incubated for 2 hours at room temperature with a biotinylated goat anti-rabbit secondary antibody (Dako, 1:500 in blocking solution). Cells were washed 3 times and incubated for 30 minutes with streptavidin Cy3 (Sigma, 1:500). All samples were sequentially washed and incubated with a mouse monoclonal anti-human CD31 (Dako, M0823, 1:100) and Alexa488-conjugated goat anti-mouse secondary antibody (ThermoFisher, 1:100), both for 1 hour at room temperature. Finally, slides were washed in PBS and incubated with DAPI (1:2000) for 5 minutes at room temperature for nuclear staining. Slides were mounted using the Prolong Gold anti-fade mounting reagent (ThermoFisher) and cured overnight. For each condition, 5 to 6 independent frames were captured for the Cy3, Alexa488 and DAPI channels using a 20X objective and a LSM510 Meta confocal microscope (Carl Zeiss Inc., Thornwood, NY) in the Wilmer Eye Institute Imaging Core Facility. Quantification of phospho-H2AX+ foci within $DAPI^+$ nuclei of $CD31^+$

VP was performed using the NIS-Elements software. Briefly, thresholds and masks were sequentially created for the Alexa488 (CD31) and DAPI channels to limit the analysis to nuclei of VP cells. Nuclei were further defined using the size/area and circularity parameters. Each individual $CD31^+$ nucleus was characterized as a single object using the "object count" function. Finally, the number of foci per nucleus was determined by counting the number of objects in the Cy3 channel. A total of 128 to 165 nuclei were analyzed for each condition (E8 vs LIF-3i ±NCS).

Ocular I/R Injury and VP Injections into (NOD/Shi-*scid*/IL-2Rγ^{null}) NOG eyes. This I/R ocular injury model was described previously [7]. Briefly, six- to eight-week old male NOG mice (Johns Hopkins Cancer Center Animal Facility) were subjected to high intraocular pressure to induce retinal ischemia-reperfusion injury. Mice were deep anesthetized by intraperitoneal (IP) injection of ketamine/xylazine (50 mg/kg ketamine + 10 mg/kg xylazine in 0.9% NaCl). The pupils were dilated with 2.5% phenylephrine hydrochloride ophthalmic solution (AK-DILATE, Akorn, Buffalo Glove, IL) followed by 0.5% tetracaine hydrochloride ophthalmic topical anesthetic solution (Phoenix Pharmaceutical, St. Joseph, MO). The anterior chamber of the eye was cannulated under microscopic guidance (OPMI VISU 200 surgical microscope, Zeiss, Gottingen, Germany) with a 30-gauge needle connected to a silicone infusion line providing balanced salt solution (Alcon Laboratories, Fort Worth, TX); avoiding injury to the corneal endothelium, iris, and lens. Retinal ischemia was induced by raising intraocular pressure of cannulated eyes to 120 mmHg for 90 min by elevating the saline reservoir. Ischemia was confirmed by iris whitening and loss of retinal red reflex. Anesthesia was maintained with two doses of 50 µL intramuscular ketamine (20 mg/mL) for up to 90 min. The needle was subsequently withdrawn, intraocular pressure normalized, and reperfusion of the retinal vessels confirmed by reappearance of the red reflex. The contralateral eye of each animal served as a non-ischemic control. Antibiotic ointment (Bacitracin zinc and Polymyxin B sulfate, AK-Poly-Bac, Akron) was applied topically. Two days later, MACS-purified and expanded human VP were injected into the vitreous body (50,000 cells in 2 µL/eye), using a micro-injector (PLI-100, Harvard Apparatus, Holliston, MA).

Whole mount immunofluorescence staining of I/R-injured NOG retinas. Human cell engraftment into NOG mouse retinas was detected directly with anti-human nuclear antigen

(HNA) immunohistochemistry with murine vascular marker co-localization (murine CD31 and collagen IV) using anti-murine CD31 and anti-murine collagen IV antibodies. Animals were euthanized for retinal harvests and HNA-positive cell quantitation at 1, 3, and 4 weeks following human VP injection (2 days post-I/R injury). After euthanasia, eyes were enucleated, cornea and lens were removed, and the retina was carefully separated from the choroid and sclera. Retinae were fixed in 2% paraformaldehyde in TBS for overnight at 4°C, and permeabilized via incubation with 0.1% Triton-X-100 in TBS solution for 15 min at 4°C. Following thorough TBS washes, free floating retinas were blocked with 2% normal goat serum in TBS with 1% bovine serum albumin and incubated overnight at 4°C in primary antibody solutions: rabbit anti-mouse Collagen IV (AB756P, Millipore, 1:100) and/or rat anti-mouse CD31 (550274, BioSciences, 1:50) in 0.1% Triton-X-100 in TBS solution (to label basement membrane and EC of blood vessels, respectively). On the next day, retinas were washed with TBS, and incubated with secondary antibodies for 6 hours at 4°C. A goat anti-rabbit Cy3-conjugated secondary antibody (Jackson Immuno Research, # 111-165-003, 1:200) was used to detect collagen IV primary antibody, and a goat anti-rat Alexafluor-647-conjugated secondary antibody (Invitrogen, # A21247, 1:200) was used to detect the anti-CD31 primary antibody. Human cells were detected using directly Cy3-conjugated anti-HNA (Millipore, MAB1281C3, 1:100). After washing in TBS, flat mount retinas were imaged with confocal microscopy (LSM510 Meta, Carl Zeiss Inc., Thornwood, NY) at the Wilmer Eye Institute Imaging Core Facility.

Immunofluorescent confocal microscopy and quantitation of human cell engraftment in murine retinae. For quantification of HNA^+ cells in the superficial layers of whole retinas, whole mount retinas were prepared from the eyes of animals at 1, 3 or 4 weeks following intra-vitreal transplantation of human cells (50,000 cells per eye) following injuries induced by I/R injury. Non-I/R injured eyes and control PBS-injected eyes were analyzed as controls. All samples were co-immunostained with anti-mouse CD31, anti-mouse collagen type IV, and human-specific anti-HNA antibodies, as described above. Images were acquired with ZEN software using a 10X objective and a LSM510 Meta confocal microscope. For each individual eye, the entire retina was tile-scanned and stitched (7x7 frames, 10% overlapping).

For human cell quantification analysis, photomicrographs were processed using the Fiji distribution of imageJ. Briefly, a region of interest was created using the DAPI channel and the "magic wand" function to conservatively delineate the whole retina and exclude from the analysis the limited background at the edges of the retina preparation that could be detected in the Cy3 (HNA) channel for some samples. The Cy3 channel was processed with the "smooth" function and a mask was created using by thresholding. The Cy3 channel was further prepared for the "analyze particle" plugin by using standardized sequential corrections that were limited to despeckle, filtering (Minimum) and watersheding. Particle objects corresponding to HNA+ nuclei were automatically counted using fixed size and circularity parameters.

Eyes were analyzed for quantification of human $CD34^+$ or human $CD31^+$ blood vessels within defined layers of the mouse retina. Briefly, the anterior eye (cornea/iris) was dissected free by a circumferential cut at the limbus. Eyecups were fixed using paraformaldehyde and prepared for cryopreservation by immersion in gradients of sucrose (Lutty et al IOVS 1993, PMID: 7680639). Eyes were hemisected through the optic nerve and the two halves embedded in OCT-sucrose. Serial cryosections (8μm thickness) were prepared once sections had the retina from ora serrata to ora serrata (**Fig S6d**), and stored at -80°C. Equally interspaced microsections [n=11 (E8) and 13 (LIF-3i) for CD34, and n=3 (E8) and 7 (LIF-3i) for CD31 immunostainings]. Retinal sections were sequentially immunostained with mouse anti-human CD34 (BD Biosciences, clone My10, #347660, 1:50) or mouse anti-human CD31 (Dako, M0823, 1:50) overnight at 4°C and then goat anti-mouse Alexa488 (ThermoFisher Scientific, 1:200) for 1 hour at room temperature, followed by rabbit anti-mouse collagen type IV (Millipore, AB756P, 1:200) or rat anti-mouse CD31 (BD Biosciences, 550274, 1:50) for 1 hour at room temperature and Alexa647-conjugated goat-anti rabbit or goat anti-rat secondary antibodies highly cross-adsorbed against IgG from other species (ThermoFisher Scientific, 1:200) for 1 hour at room temperature. Finally, sections were blocked for 30 minutes with mouse serum and immunostained with directly Cy3-conjugated anti-human HNA (Millipore, MAB1281C3, 1:100). Nuclei were counterstained using DAPI. Primary antibodies were replaced by mouse, rat and rabbit nonimmune IgG (Dako or ThermoFisher Scientific) at the corresponding antibody concentration to verify absence of unspecific antibody binding. Retinal sections were mounted with Prolong Gold anti-fade reagent

(ThermoFisher Scientific) and cured overnight in the dark. Images were acquired using a 20X objective with the ZEN software and a LSM510 Meta confocal microscope. Photomicrographs were further processed for quantification using the Fiji distribution of imageJ. Briefly, regions of interest were created using the DAPI channel as a template to delineate the GCL, INL, and ONL, the other regions (ILM, IPL, OPL and S) being defined as intercalated around and between the 3 DAPI-defined ROIs. Analysis was pursued by processing the Alexa488 (human CD34 or CD31) channel using a sequential series of defined parameters using the "smooth", "despeckle", "filter (median)" functions and thresholding. Alexa488^{+} objects were counted within and between ROIs using the "analyzes particles" plugin.

Quantitative Real-time Polymerase Chain Reaction (qRT-PCR) and ChIP-PCR. The sequences and published reference citations of all PCR primers used in these studies for qRT-PCR and qChIP-PCR are listed in **Table S3.** For qRT-PCR analyses, feeder-dependent LIF-3i hPSC cultures were MEF-depleted by pre-plating onto 0.1% gelatin-coated plates for 1 hour at 37°C, as previously described [12]. Samples were sequentially and simultaneously collected from representative hPSC lines in primed (E8), or naïve (LIF-3i; p>3) conditions. Alternatively, isogenic paired samples were prepared from EGM2-expanded primed and naïve VP. Total RNA was isolated from snap-frozen samples using the RNeasy Mini Kit (Qiagen) following the manufacturer's instructions, and quantified using a Nanodrop spectrophotometer (ThermoFisher Scientific). Genomic DNA was eliminated by in-column DNase (Qiagen) digestion. Reverse transcription of RNA (1µg/sample) was accomplished using the SuperScript VILO cDNA Synthesis Kit (ThermoFisher Scientific) and a MasterCycler EPgradient (Eppendorf). For real-time PCR amplification, diluted (1:20) cDNA samples were admixed to the TaqMan Fast Advanced Master Mix (ThermoFisher Scientific) and Taqman gene expression assays (ThermoFisher Scientific).

Matching samples were prepared in parallel for ChIP-PCR assays. Isogenic hPSC cultures were expanded using primed (E8) and naïve (LIF-3i/MEF) conditions and analyzed at passages matching RT-PCR analysis. Alternatvely, VP cells were prepared from isogenic primed and naïve PSC using the same APEL/EGM2 conditions as the samples prepared for RT-PCR. Cells were collected using Accutase and counted using a Countess cell counter

(ThermoFisher Scientific). Feeders were excluded from LIF-3i/MEF samples by pre-plating for 1 hour on gelatin-coated plates and pre-plated samples were re-counted after the pre-plating step. 3 x10^6 cells were allocated per ChIP assay and prepared using the Magna ChIP A/G chromatin immunoprecipitation kit (Millipore). Cells were centrifuged (300g), supernatant was discarded and cells were fixed for 10 minutes at room temperature by resuspending in 1mL of PBS, 1% formaldehyde (Affymetrix). Unreacted formaldehyde was quenched using 100μL 10X Glycine (Millipore). Samples were left at room temperature for 5 minutes, centrifuged (300g) and washed twice in 1mL ice-cold PBS. Samples were resuspended in ice-cold PBS containing either 1X Protease Inhibitor Cocktail II (Millipore) or 1X complete Mini protease inhibitor (Roche). Samples were centrifuged at 800g for 5 minutes, cell pellets were snap-frozen in liquid nitrogen and stored at -80°C until use for ChIP assay. Cell lysis, homogenization and nuclear extraction of cryopreserved samples were processed using the reagents provided in the Magna ChIP kit and the manufacturer instructions. The isolated chromatin was fragmented using a Diagenode Bioruptor Plus sonication device. Sonication settings (10 cycles, high, 30s on, 30s off) were validated in pilot experiments to shear cross-linked DNA to 200-1000 base pairs by agarose gel electrophoresis. The sheared chromatin was centrifuged at 10,000g at 4°C for 10 minutes and immediately processed for immunoprecipitation. 1x10^6 cell equivalent of cross-linked sheared chromatin were prepared according to the kit manufacturer's protocol. Briefly, 1% of sheared chromatin was separated as "input" control. The remaining sample was admixed with 5 μg of immunoprecipitating antibody (**Table S3**) and protein A/G magnetic beads. Antibodies were substituted with corresponding rabbit or mouse IgG (**Table S3**) as negative isotype controls using 5% sheared chromatin. The chromatin-antibody-beads mixture was left incubating overnight at 4°C with agitation. Protein A/G beads were pelleted using a MagJET separation rack (ThermoFisher Scientific) and supernatant was discarded. Protein/DNA complexes were washed and eluted, beads were separated using the MagJET rack and DNA was purified according to the manufacturer's instructions. The immunoprecipitated genomic DNA was amplified using the Power SYBR Green Master Mix (ThermoFisher Scientific) with relevant published primers for GAPDH, GATA2, GATA6, HAND1, NANOG, MSX2, PAX6, SOX1 (**Table S3**), CD31, vWF, endothelin-1, ICAM2, MYOD1 (all from [1]), CXCR4, DLL1, FZD7 and ELP3 (all from reference [65]) (**Table S3**) using a ViAA7 Real Time PCR System

(ThermoFisher Scientific). Specificity of antibodies was validated using the isotype controls and samples were normalized to their corresponding input controls.

Genomic DNA dot-blots of 5MC and 5hMC CpG methylation. Genomic DNA from isogenic parallel primed (E8) and preplated LIF-3i cultures of representative hiPSC lines was extracted using the DNeasy Blood and tissue Kit (Qiagen) and quantified using a Nanodrop spectrophotometer (ThermoFisher Scientific), as described [12]. For each sample, 1.6μg DNA was diluted in 50μL of nuclease-free water (Ambion), denatured by adding 50μL of 0.2M NaOH, 20mM EDTA and incubating for 10 minutes at 95°C, and neutralized by adding 100μL 20X Saline-Sodium Citrate SSC hybridization buffer (G Biosciences) and chilling on ice. A series of five 2-fold dilutions (800ng to 50ng) and nuclease-free water controls were spotted on a pre-wetted (10X SSC buffer) nylon membrane using a Bio-Dot Microfiltration Apparatus (Bio-Rad). The blotted membrane was air-dried and UV-cross-linked at 1200 J/m^2 using a UV Stratalinker 1800 (Stratagene). The membrane was blocked in TBST, 5% nonfat dry milk for 1 hour at room temperature with gentle agitation, washed 3 times in TBST, and incubated at 4°C overnight with rabbit anti-5mC (Cell Signaling, 1:1000) or anti-5hmC (Active Motif, 1:5000) antibodies diluted in TBST, 5% BSA. The membrane was washed 3 times in TBST and incubated for 1 hour at room temperature with HRP-conjugated anti-rabbit secondary antibody (Cell Signaling) diluted 1:1000 in blocking buffer. After 3 washes in TBST, the membrane was treated with Pierce ECL Substrate (ThermoFisher) for chemiluminescent detection using an Amersham Imager 600 (Amersham). After acquisition, the membrane was washed 3 times in water and immersed in 0.1% methylene blue (Sigma), 0.1M sodium acetate stain solution for 10 minutes at room temperature. Excess methylene blue was washed 3 times in water with gentle agitation. Colorimetric detection was achieved using the Amersham Imager 600 (Amersham). 5mC, 5hmC and methylene blue intensities were quantified by ImageJ software.

Bioinformatics Analyses. The (Illumina, San Diego, CA gene expression arrays (Illumina Human HT-12 Expression BeadChip) and Infinium 450K CpG methylation raw array data analyzed in these studies were published previously and available at Gene Expression Omnibus under accession numbers GSE65211 and GSE65214, respectively, and processed as previously described [12]. Gene specific enrichment analysis (GSEA) of expression arrays was conducted as described [66]. The bioinformatics method for calculating crossplots of

differential promoter CpG methylation beta values *vs.* corresponding differential gene expression was previously described [12].

ACKNOWLEDGEMENTS

This work was supported by grants from the NIH/NEI (R01EY023962), NIH/NICHD (R01HD082098), Novo-Nordisk Diabetes & Obesity Science Forum Award, RPB Stein Innovation Award, The Maryland Stem Cell Research Fund (2018-MSCRFV-4048, 2014-MSCRFE-118153), an RPB Unrestricted grant (Wilmer), The Lisa Dean Moseley Foundation, and Wilmer core grant for vision research (EY001765). We are grateful for technical support by Jessica Davidson.

AUTHOR CONTRIBUTIONS

TSP, LZ, and ETZ designed all experiments and wrote manuscript. TSP, LZ, REM, JT, JSH, RK, AH, NR, SM, RG, and IB performed and analyzed experiments. All authors edited the manuscript, interpreted results, and gave final approval of the manuscript. ETZ supervised and directed the studies.

COMPETING INTERESTS

Authors do not declare any competing financial interests.

SUPPLEMENTAL INFORMATION

Accompanies this manuscript at the following weblink:

FIGURE LEGENDS

Figure 1. **Multi-lineage teratoma organoid quantifications in primed vs. naïve hiPSC**. The human fibroblast-hiPSC line C1.2 was cultured in parallel in either conventional E8 or LIF-3i/MEF conditions prior to injection into sibling NOG mice ($5x10^6$ cells/site) for teratoma assays. Paraffin sections of 8-week-old teratomas were evaluated with (**a, b**) H&E staining, or (**c, d**) immunofluorescence (IF) staining for markers of endodermal (Cytokeratin8$^+$ (CK8) gut/glandular structures), mesodermal (NG2+ chondroblasts), and ectodermal (SOX2$^+$ neural rosettes) lineages along with the proliferation marker Ki67, as described in Methods. Scale Bar = 50μm. ** = p< 0.01; *** = p < 0.001.

Figure 2. **Characterization of conventional and LIF-3i-reverted diabetic hiPSC lines**. (**a**) Immunofluorescent staining of N-DhiPSC line E1C1 following LIF-3i reversion for pluripotency (TRA-1-81, NANOG, OCT4) and naïve-specific proteins (KLF2, NR5A2, TFCP2L1, STELLA/DPPA3, E-CADHERIN; Scale Bar = 50μm). Isogenic lysates were prepared from DhiPSC lines (E1C1, E1CA1, E1CA2), hESC line (H9), or normal fibroblast-hiPSC lines (C1.2, C2) from conventional E8 *vs*. LIF3i cultures. Western blots were performed for (**b**) XAV939-inhibited proteolysis of tankyrases 1 and 2 (TANK ½) and AXIN-1, (**c**) naïve-specific expression of pluripotency factor TFAP2C [31], and (**d**) expressions of phosphorylated (P-STAT3) and total STAT3 (T-STAT3). (**e**) Teratoma organoid quantifications in primed DhiPSC (blue bar), vs N-DhiPSC, line E1CA2 (red bar). Quantification of mesodermal (NG2$^+$ chondroblast), definitive endodermal (CK8$^+$ gut/glandular cells), and ectodermal (SOX2+ neural rosettes; retinal pigmented epithelium by H&E staining). * = p< 0.05; *** = p < 0.001.

Figure 3. **Primed vs naïve vascular differentiations of non-diabetic and diabetic patient-derived hiPSC**. (**a**) Schematic timeline of vascular differentiation using defined xeno-free APEL medium supplemented with the indicated growth factors and inhibitor molecules. Day 7 differentiated VP cells were enriched for CD31 expression using magnetic-activated cell sorting (MACS); CD31$^+$ VP co-express CD146 post-MACS enrichment (*i.e.*, CD31$^+$CD146$^+$ VP). CD31$^+$CD146$^+$ VP were further expanded in EGM2 medium prior to in vitro characterization or injection into I/R-injured NOG-SCID eyes. (**b**) Kinetics of mRNA

expression for the VP markers *TIE1* and *TIE2* in APEL between day 0 and day 12 of differentiation starting from isogenic primed (blue) and naïve (red) cultures of the representative CB-hiPSC line 6.2 by Q-RT-PCR. (**c**) Kinetics of protein surface marker expressions of pluripotency (SSEA4, TRA-1-81) and vascular (CD31, CD146, CD34, CD144) markers from isogenic primed (blue) and naïve (red) DhiPSC lines (E1C1, E1CA1; n=2). (**d**) Average percentage of $CD31^{+}CD146^{+}$ cells obtained from APEL differentiations of isogenic non-diabetic and diabetic hiPSC on the day of CD31+ sorting (day 7-8). Representative results are shown for differentiation of the non-diabetic CB-iPSC line E5C3 and 2 D-iPSC lines (E1CA1, E1CA2) starting from simultaneous and isogenic primed E8 (-) and naïve LIF-3i/MEF (+) cultures. (**e**) Transmission electron microscopy (TEM) images of VP differentiated and expanded from parallel E8- and LIF3i cultures of the D-hiPSC line E1C1. WPB: Weibel-Palade body, n: nucleus, TEC: transcytotic endothelial channel; Scale Bar = 400nm.

Figure 4. **Characterization of purified and expanded VP from primed *vs*. naïve hiPSC**. (**a**) Detection of CD31 transcripts by qRT-PCR in starting diabetic (D) and non-diabetic (N) fibroblasts, in undifferentiated primed (E8) and naïve (LIF-3i) hESC (RUES01) and DhiPSC (E1CA2) and in APEL-differentiated $CD31^{+}CD146^{+}$ VP that were FACS-purified, and re-plated and expanded in EGM2. VP populations were derived from isogenic primed (E8) and naïve (LIF-3i) hESC (RUES01) or DhiPSC (E1CA2). (**b**) Quantification of vascular tube lengths formed from *in vitro* Matrigel tube assays from primed vs naïve D-iPSC-VP. (**c**) Flow cytometrical quantification of acetylated-Dil-LDL (Ac-DI-LDL) uptake in VP cells that were derived from primed vs naïve isogenic CB-hiPSC and DhiPSC lines. (**d**) Representative flow cytometry (left panel) and immunofluorescence detection in LDL uptake assays (right panel); merged phase contrast/ Ac-Dil-LDL-labeled VP cells; Scale Bar = 100μm. (**e**) EdU proliferation assays of purified VP after 4 passages in EGM2 post-$CD31^{+}$ purification. N-D-iPSC-VP demonstrated higher proliferative capacity up to passage 3 compared to isogenic primed cells. (**f**) Expanded VP (3-6 passages) were quantitated for senescent cells by β-galactosidase activity colorimetric assay. Shown are isogenic comparisons of both non-diabetic hPSC-VP (H9 hESC, C1.2, C2 fibroblast-hiPSC lines) and DhiPSC-VP (E1CA1, E1CA2, E1C1 lines).

Figure 5. **DNA damage responses in primed vs naïve D-iPSC-VP**. (**a**) purified and expanded CD31$^+$ VP were treated with the radiomimetic NCS for 5 hours before fixation and staining with antibodies for detection of human CD31$^+$ cells and phosphorylated H2AX (pH2AX) positive foci that revealed double-strand DNA breaks (arrows); Scale Bar = 50μm. (**b**) Quantification of pH2AX foci per nuclei in isogenic primed (E8) and naïve (LIF-3i DhiPSC with or without induction of DNA damage with NCS. Shown are numbers of nuclei per field with no pH2AX foci (green), and nuclei with (1-5; light pink), (6-10; dark pink) and >10 pH2AX foci (red). (**c**) Lysates of primed (E8) and naïve (LIF-3i) D-iPSC-derived VP were collected with and without supplementing EGM2 with NCS for 5 hours and analyzed expressions of proteins activated by DNA damage and apoptosis (phosphorylated H2AX (P-H2AX), RAD51, RAD54, and phosphorylated p53 (P-p53).

Figure 6. **Survival of primed *vs*. naïve diabetic VP in I/R-injured murine retinas**. (**a**) Three weeks following injection of primed or naïve DhiPSC-derived VP into the vitreous of I/R-treated NOG mice, whole retinae were stained with antibodies for detection of murine CD31 (mCD31, green), collagen IV (mCol-IV), and human-specific HNA (red), and flat whole-mounted for tile scanning by confocal microscopic imaging (10x objective, 9x9 tiles). Shown are HNA$^+$ cells primed (E8)-VP injected (left panel) *vs*. naïve (LIF-3i) VP-injected (right panel) retinae. Scale bars = 500 μm. (**b**) Higher magnification of retinal vascular regions demonstrated HNA$^+$ DhiPSC-VP cells were located either abundantly within vitreous or engrafted into vascular abluminal regions of murine ischemic vessels (arrow heads); Scale bars = 50 μm. Quantitation of HNA$^+$ cells in outer superficial layers of whole mount retinae following treatment of eyes with and without I/R, and injected with either primed VP or naïve VP at 1 week (**d**) and 4 weeks (**e**) following injections. Shown are the mean numbers total HNA+ cells counted per each retina (field) of individual experiments (n=3).

Figure 7. **Vascular engraftment of primed *vs*. naïve diabetic VP in I/R-injured murine neural retinal blood vessels**. Whole mount retinae of I/R injured eyes of NOG mice were immuno-stained with either human CD34 (**a**, hCD34) or human CD31 (hCD31) antibodies to detect human endothelial cells at 2 weeks after VP injections. Antibodies for murine collagen type-IV (mCol-IV) were employed to detect murine blood vessel basement membrane, and murine CD31 (mCD31) detected murine endothelium. The number of human CD34$^+$ (**b**) or

(**c**) human CD31$^+$ cells detected within all transverse layers of the murine neural retina (per 450μm retinal cross section; see **Fig. S6d**) was quantitated 2 weeks after injection into ischemia-injured eyes. Each data point represents a replicate individual 450μm retinal cross section that was analyzed from I/R- treated eyes injected with saline (PBS), primed VP (E8), or naïve VP (L3i). Human CD34$^+$ (**d, e**) or human CD31$^+$ (**f, g**) endothelial cell engraftment was enumerated in each distinct layer of neural retina shown, and demonstrated that only N-DhiPSC-VP migrated into the inner nuclear layer (INL) while most of the primed-D-iPSC-VP remained in the superficial ganglion cell layer (GCL). ILM: inner limiting membrane, IPL: inner plexiform layer, outer nuclear layer (ONL), OPL: outer plexiform layer, S: segments. All scale bars = 50 μm.

Figure 8. Epigenetic configurations of multi-lineage bivalent and vascular lineage-specific promoters in primed vs naïve hiPSC and VP. (**a**) Crossplot of mean genome-wide gene expression of PRC2 module gene targets (**Table S3**) *vs.* CpG methylation of non-diabetic N-hiPSC *vs.* their isogenic primed isogenic hiPSC counterparts (*n*=6 hiPSC lines). Plotted are the differentially methylated region (DMR) CpG methylation beta values of PRC2 module promoter regions in LIF-3-reverted hiPSC minus their isogenic primed hPSC counterparts (y-axis, p ≤0.05) *vs*. their corresponding differential gene expressions for the same genes (red, x-axis, $\log_2$ fold changes (FC); p ≤ 0.05, FC +/- ≥1.5.). **(b)** Curated GSEA pathways for gene targets of the PRC2 module over-represented (FDR<0.01; p<0.001) in LIF-3i-reverted fibroblast-hiPSC *vs*. their isogenic primed counterparts (*n*=3 hiPSC lines). (**c**) Western blot analysis of PRC2 components EZH1, EZH2, SUZ12, and JARID2) in primed vs naïve hiPSC lysates; E1C1 fibroblast-DhiPSC line; C1.2 normal donor fibroblast-hiPSC line. (**d**) ChiP-qPCR for H3K27me3 and H3K4me3 histone marks at key known bivalent developmental promoters in primed vs naïve DhiPSC (*e.g*., PAX6, MSX2, GATA6, SOX1, HAND1, GATA2). Levels of GAPDH and NANOG are controls for actively transcribed genes. Data is presented as *differences* in percent input materials of naïve minus primed genomic DNA samples for DhiPSC line E1C1 (see **Fig S8c**). Bars represent the SEM of replicates. (**e**) ChiP-qPCR for H3K27me3 and H3K4me3 histone marks at key vascular developmental promoters in primed vs naïve VP genomic samples. Data is presented as GAPDH-normalized ratios of percent input materials between naïve and primed VP differentiated from the DhiPSC line E1C1. Results are shown as ratios of isogenic LIF-3i N-D-hiPSC-VP vs E8

D-hiPSC for GATA2-regulated genes (CD31, vWF, endothelin-1, ICAM2) and genes regulated by histone marks that are known to effect vascular functionality (CXCR4, DLL1, FZD7). The histone profile for GAPDH is a 'housekeeping control gene. NANOG and MYOD1 are control gene promoters that become repressed during vascular differentiation. (**f**) qRT-PCR gene expression analysis of vascular lineage genes (left panel) and PRC2-regulated bivalent lineage-specific genes (right panel) in D-hiPSC-derived VP that were differentiated from isogenic pairs of naive vs primed D-hiPSC lines (*n*=3; lines E1C1, E1CA1, E1CA2). Fold changes are normalized to beta-actin expression. All PCR primers are listed in **Table S3**.

REFERENCES

1 Lutty, G. A. Diabetic choroidopathy. *Vision Res* **139**, 161-167, doi:10.1016/j.visres.2017.04.011 (2017).

2 Zheng, L., Gong, B., Hatala, D. A. & Kern, T. S. Retinal ischemia and reperfusion causes capillary degeneration: similarities to diabetes. *Invest Ophthalmol Vis Sci* **48**, 361-367, doi:10.1167/iovs.06-0510 (2007).

3 Joussen, A. M. *et al.* A central role for inflammation in the pathogenesis of diabetic retinopathy. *FASEB J* **18**, 1450-1452, doi:10.1096/fj.03-1476fje (2004).

4 Joussen, A. M. *et al.* Leukocyte-mediated endothelial cell injury and death in the diabetic retina. *Am J Pathol* **158**, 147-152, doi:10.1016/S0002-9440(10)63952-1 (2001).

5 D'Amore, P. A. Mechanisms of retinal and choroidal neovascularization. *Invest Ophthalmol Vis Sci* **35**, 3974-3979 (1994).

6 Glaser, B. M., D'Amore, P. A., Michels, R. G., Patz, A. & Fenselau, A. Demonstration of vasoproliferative activity from mammalian retina. *J Cell Biol* **84**, 298-304, doi:10.1083/jcb.84.2.298 (1980).

7 Park, T. S. *et al.* Vascular progenitors from cord blood-derived induced pluripotent stem cells possess augmented capacity for regenerating ischemic retinal vasculature. *Circulation* **129**, 359-372, doi:10.1161/CIRCULATIONAHA.113.003000 (2014).

8 Dar, A. *et al.* Multipotent vasculogenic pericytes from human pluripotent stem cells promote recovery of murine ischemic limb. *Circulation* **125**, 87-99, doi:10.1161/CIRCULATIONAHA.111.048264 (2012).

9 Mandai, M., Kurimoto, Y. & Takahashi, M. Autologous Induced Stem-Cell-Derived Retinal Cells for Macular Degeneration. *N Engl J Med* **377**, 792-793, doi:10.1056/NEJMc1706274 (2017).

10 Sharma, R. *et al.* Clinical-grade stem cell-derived retinal pigment epithelium patch rescues retinal degeneration in rodents and pigs. *Sci Transl Med* **11**, doi:10.1126/scitranslmed.aat5580 (2019).

11 Zimmerlin, L., Park, T. S. & Zambidis, E. T. Capturing Human Naive Pluripotency in the Embryo and in the Dish. *Stem Cells Dev* **26**, 1141-1161, doi:10.1089/scd.2017.0055 (2017).

12 Zimmerlin, L. *et al.* Tankyrase inhibition promotes a stable human naive pluripotent state with improved functionality. *Development* **143**, 4368-4380, doi:10.1242/dev.138982 (2016).

13 Park, T. S., Zimmerlin, L., Evans-Moses, R. & Zambidis, E. T. Chemical Reversion of Conventional Human Pluripotent Stem Cells to a Naive-like State with Improved Multilineage Differentiation Potency. *J Vis Exp*, doi:10.3791/57921 (2018).

14 Brunner, S. *et al.* Circulating angiopoietic cells and diabetic retinopathy in type 2 diabetes mellitus, with or without macrovascular disease. *Invest Ophthalmol Vis Sci* **52**, 4655-4662, doi:10.1167/iovs.10-6520 (2011).

15 Caballero, S. *et al.* Ischemic vascular damage can be repaired by healthy, but not diabetic, endothelial progenitor cells. *Diabetes* **56**, 960-967, doi:10.2337/db06-1254 (2007).

16 Jarajapu, Y. P. & Grant, M. B. The promise of cell-based therapies for diabetic complications: challenges and solutions. *Circ Res* **106**, 854-869, doi:10.1161/CIRCRESAHA.109.213140 (2010).

17 Khullar, M., Cheema, B. S. & Raut, S. K. Emerging Evidence of Epigenetic Modifications in Vascular Complication of Diabetes. *Front Endocrinol (Lausanne)* **8**, 237, doi:10.3389/fendo.2017.00237 (2017).

18 Manzar, G. S., Kim, E. M. & Zavazava, N. Demethylation of induced pluripotent stem cells from type 1 diabetic patients enhances differentiation into functional pancreatic beta cells. *J Biol Chem* **292**, 14066-14079, doi:10.1074/jbc.M117.784280 (2017).

19 Yang, J. *et al.* Establishment of mouse expanded potential stem cells. *Nature* **550**, 393-397, doi:10.1038/nature24052 (2017).

20 Kim, H. *et al.* Modulation of beta-catenin function maintains mouse epiblast stem cell and human embryonic stem cell self-renewal. *Nat Commun* **4**, 2403, doi:10.1038/ncomms3403 (2013).

21 Gao, X. *et al.* Establishment of porcine and human expanded potential stem cells. *Nat Cell Biol* **21**, 687-699, doi:10.1038/s41556-019-0333-2 (2019).

22. Theunissen, T.W., et al., *Molecular Criteria for Defining the Naive Human Pluripotent State.* Cell Stem Cell, 2016.

23. Pastor, W.A., et al., *Naive Human Pluripotent Cells Feature a Methylation Landscape Devoid of Blastocyst or Germline Memory.* Cell Stem Cell, 2016. **18**(3): p. 323-9.

24. Choi, J., et al., *Prolonged Mek1/2 suppression impairs the developmental potential of embryonic stem cells.* Nature, 2017. **548**(7666): p. 219-223.

25. Warrier, S., et al., *Direct comparison of distinct naive pluripotent states in human embryonic stem cells.* Nat Commun, 2017. **8**: p. 15055.

26. Lee, J.H., et al., *Lineage-Specific Differentiation Is Influenced by State of Human Pluripotency.* Cell Rep, 2017. **19**(1): p. 20-35.

27 Park, T. S. *et al.* Growth factor-activated stem cell circuits and stromal signals cooperatively accelerate non-integrated iPSC reprogramming of human myeloid progenitors. *PLoS ONE* **7**, e42838, doi:10.1371/journal.pone.0042838 (2012).

28 Burridge, P. W. *et al.* A universal system for highly efficient cardiac differentiation of human induced pluripotent stem cells that eliminates interline variability. *PLoS ONE* **6**, e18293, doi:10.1371/journal.pone.0018293 (2011).

29 Bar-Nur, O. *et al.* Small molecules facilitate rapid and synchronous iPSC generation. *Nat Methods* **11**, 1170-1176, doi:10.1038/nmeth.3142 (2014).

30. Bai, P. Biology of poly(ADP-ribose) polymerases: the factotums of cell maintenance. (2015), *Mol Cell*, 58, 947-958, http://dx.doi.org/10.1016/j.molcel.2015.01.034

31. Pastor, W.A., et al., *TFAP2C regulates transcription in human naive pluripotency by opening enhancers. Nat Cell Biol*, 2018. **20**(5): p. 553-564.

32. Ng, E. S., Davis, R., Stanley, E. G. & Elefanty, A. G. A protocol describing the use of a recombinant protein-based, animal product-free medium (APEL) for human embryonic stem cell differentiation as spin embryoid bodies. *Nature protocols* **3**, 768-776, doi:10.1038/nprot.2008.42 (2008).

33. Orlova, V. V. *et al.* Generation, expansion and functional analysis of endothelial cells and pericytes derived from human pluripotent stem cells. *Nat Protoc* **9**, 1514-1531, doi:10.1038/nprot.2014.102 (2014).

34. Feng, Q. *et al.* Hemangioblastic derivatives from human induced pluripotent stem cells exhibit limited expansion and early senescence. *Stem Cells* **28**, 704-712, doi:10.1002/stem.321 (2009).

35. Rufaihah, A. J. *et al.* Human induced pluripotent stem cell-derived endothelial cells exhibit functional heterogeneity. *American journal of translational research* **5**, 21-35 (2013).

36. Crisan, M. A perivascular origin for mesenchymal stem cells in multiple human organs. *Cell Stem Cell* (2008).
37. Kuo, W. L., Meyn, R. E. & Haidle, C. W. Neocarzinostatin-mediated DNA damage and repair in wild-type and repair-deficient Chinese hamster ovary cells. *Cancer Res* **44**, 1748-1751 (1984).
38. Marks, H. *et al.* The transcriptional and epigenomic foundations of ground state pluripotency. *Cell* **149**, 590-604, doi:10.1016/j.cell.2012.03.026 (2012).
39 Leitch, H. G. *et al.* Naive pluripotency is associated with global DNA hypomethylation. *Nat Struct Mol Biol* **20**, 311-316, doi:10.1038/nsmb.2510 (2013).
40. Tee, W. W., Shen, S. S., Oksuz, O., Narendra, V. & Reinberg, D. Erk1/2 activity promotes chromatin features and RNAPII phosphorylation at developmental promoters in mouse ESCs. *Cell* **156**, 678-690, doi:10.1016/j.cell.2014.01.009 (2014).
41. Thornton, S. R., Butty, V. L., Levine, S. S. & Boyer, L. A. Polycomb Repressive Complex 2 regulates lineage fidelity during embryonic stem cell differentiation. *PLoS One* **9**, e110498, doi:10.1371/journal.pone.0110498 (2014).
42. Shan, Y. *et al.* PRC2 specifies ectoderm lineages and maintains pluripotency in primed but not naive ESCs. *Nat Commun* **8**, 672, doi:10.1038/s41467-017-00668-4 (2017).
43. Landeira, D. *et al.* Jarid2 is a PRC2 component in embryonic stem cells required for multi-lineage differentiation and recruitment of PRC1 and RNA Polymerase II to developmental regulators. *Nat Cell Biol* **12**, 618-624, doi:10.1038/ncb2065 (2010).
44. Fraineau, S. *et al.* Epigenetic Activation of Pro-angiogenic Signaling Pathways in Human Endothelial Progenitors Increases Vasculogenesis. *Stem Cell Reports* **9**, 1573-1587, doi:10.1016/j.stemcr.2017.09.009 (2017).
45. Yang, Y. *et al.* Derivation of Pluripotent Stem Cells with In Vivo Embryonic and Extraembryonic Potency. *Cell* **169**, 243-257 e225, doi:10.1016/j.cell.2017.02.005 (2017).
46. Guo, G. *et al.* Epigenetic resetting of human pluripotency. *Development* **144**, 2748-2763, doi:10.1242/dev.146811 (2017).
47. Bhardwaj, A., Yang, Y., Ueberheide, B. & Smith, S. Whole proteome analysis of human tankyrase knockout cells reveals targets of tankyrase-mediated degradation. *Nature communications* **8**, 2214, doi:10.1038/s41467-017-02363-w (2017).
48. Schneider, R. P. *et al.* TRF1 is a stem cell marker and is essential for the generation of induced pluripotent stem cells. *Nature communications* **4**, 1946, doi:10.1038/ncomms2946 (2013).
49. De Vos, M. *et al.* Poly(ADP-ribose) polymerase 1 (PARP1) associates with E3 ubiquitin-protein ligase UHRF1 and modulates UHRF1 biological functions. *J Biol Chem* **289**, 16223-16238, doi:10.1074/jbc.M113.527424 (2014).
50. Zampieri, M. *et al.* Parp1 localizes within the Dnmt1 promoter and protects its unmethylated state by its enzymatic activity. *PLoS One* **4**, e4717, doi:10.1371/journal.pone.0004717 (2009).
51. Vigorelli, V. *et al.* Abnormal DNA Methylation Induced by Hyperglycemia Reduces CXCR 4 Gene Expression in CD 34(+) Stem Cells. *J Am Heart Assoc* **8**, e010012, doi:10.1161/JAHA.118.010012 (2019).
52. Liao, Y. *et al.* NADPH oxidase 4 and endothelial nitric oxide synthase contribute to endothelial dysfunction mediated by histone methylations in metabolic memory. *Free Radic Biol Med* **115**, 383-394, doi:10.1016/j.freeradbiomed.2017.12.017 (2018).

53. Hou, Q., Hu, K., Liu, X., Quan, J. & Liu, Z. HADC regulates the diabetic vascular endothelial dysfunction by targetting MnSOD. *Biosci Rep* **38**, doi:10.1042/BSR20181042 (2018).
54 Incalza, M. A. *et al.* Oxidative stress and reactive oxygen species in endothelial dysfunction associated with cardiovascular and metabolic diseases. *Vascul Pharmacol* **100**, 1-19, doi:10.1016/j.vph.2017.05.005 2018).
55 Hammes, H. P. Diabetic retinopathy: hyperglycaemia, oxidative stress and beyond. *Diabetologia* **61**, 29-38, doi:10.1007/s00125-017-4435-8 (2018).
56 Wu, J. *et al.* Sodium butyrate attenuates diabetes-induced aortic endothelial dysfunction via P300-mediated transcriptional activation of Nrf2. *Free Radic Biol Med* **124**, 454-465, doi:10.1016/j.freeradbiomed.2018.06.034 (2018).
57 Xie, M. Y., Yang, Y., Liu, P., Luo, Y. & Tang, S. B. 5-aza-2'-deoxycytidine in the regulation of antioxidant enzymes in retinal endothelial cells and rat diabetic retina. *Int J Ophthalmol* **12**, 1-7, doi:10.18240/ijo.2019.01.01 (2019).
58. Carcamo-Orive, I., Huang, N. F., Quertermous, T. & Knowles, J. W. Induced Pluripotent Stem Cell-Derived Endothelial Cells in Insulin Resistance and Metabolic Syndrome. *Arterioscler Thromb Vasc Biol* **37**, 2038-2042, doi:10.1161/ATVBAHA.117.309291 (2017).
59. Chan, X. Y. *et al.* Three-Dimensional Vascular Network Assembly From Diabetic Patient-Derived Induced Pluripotent Stem Cells. *Arterioscler Thromb Vasc Biol* **35**, 2677-2685, doi:10.1161/ATVBAHA.115.306362 (2015).
60. Drawnel, F. M. *et al.* Disease modeling and phenotypic drug screening for diabetic cardiomyopathy using human induced pluripotent stem cells. *Cell Rep* **9**, 810-821, doi:10.1016/j.celrep.2014.09.055 (2014).
61. Gu, M. *et al.* Pravastatin reverses obesity-induced dysfunction of induced pluripotent stem cell-derived endothelial cells via a nitric oxide-dependent mechanism. *Eur Heart J* **36**, 806-816, doi:10.1093/eurheartj/ehu411 (2015).
62. Kikuchi, C. *et al.* Comparison of Cardiomyocyte Differentiation Potential Between Type 1 Diabetic Donor- and Nondiabetic Donor-Derived Induced Pluripotent Stem Cells. *Cell Transplant* **24**, 2491-2504, doi:10.3727/096368914X685762 (2015).
63. Stepniewski, J. *et al.* Induced pluripotent stem cells as a model for diabetes investigation. *Sci Rep* **5**, 8597, doi:10.1038/srep08597 (2015).
64. Thatava, T. *et al.* Intrapatient variations in type 1 diabetes-specific iPS cell differentiation into insulin-producing cells. *Mol Ther* **21**, 228-239, doi:10.1038/mt.2012.245 (2013).
65. Kanki, Y. *et al.* Epigenetically coordinated GATA2 binding is necessary for endothelium-specific endomucin expression. *EMBO J* **30**, 2582-2595, doi:10.1038/emboj.2011.173 (2011).
66. Subramanian, Tamayo, et al. (2005, Proc. Natl. Acad. Scie. USA, 102, 15545-15550) and Mootha, Lindgren, et al. (2003), *Nat Genet* 34, 267-273.

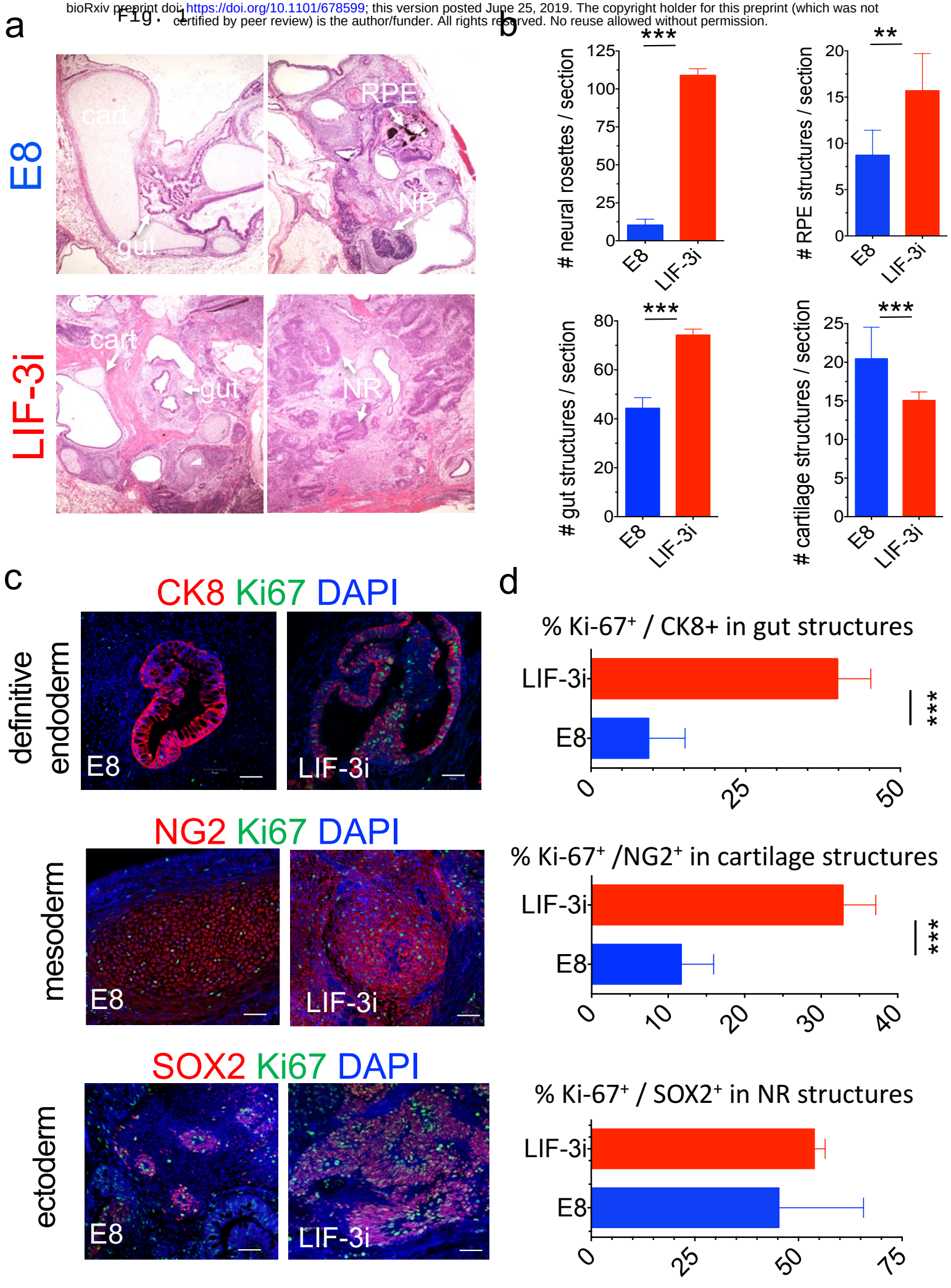

Fig. 2

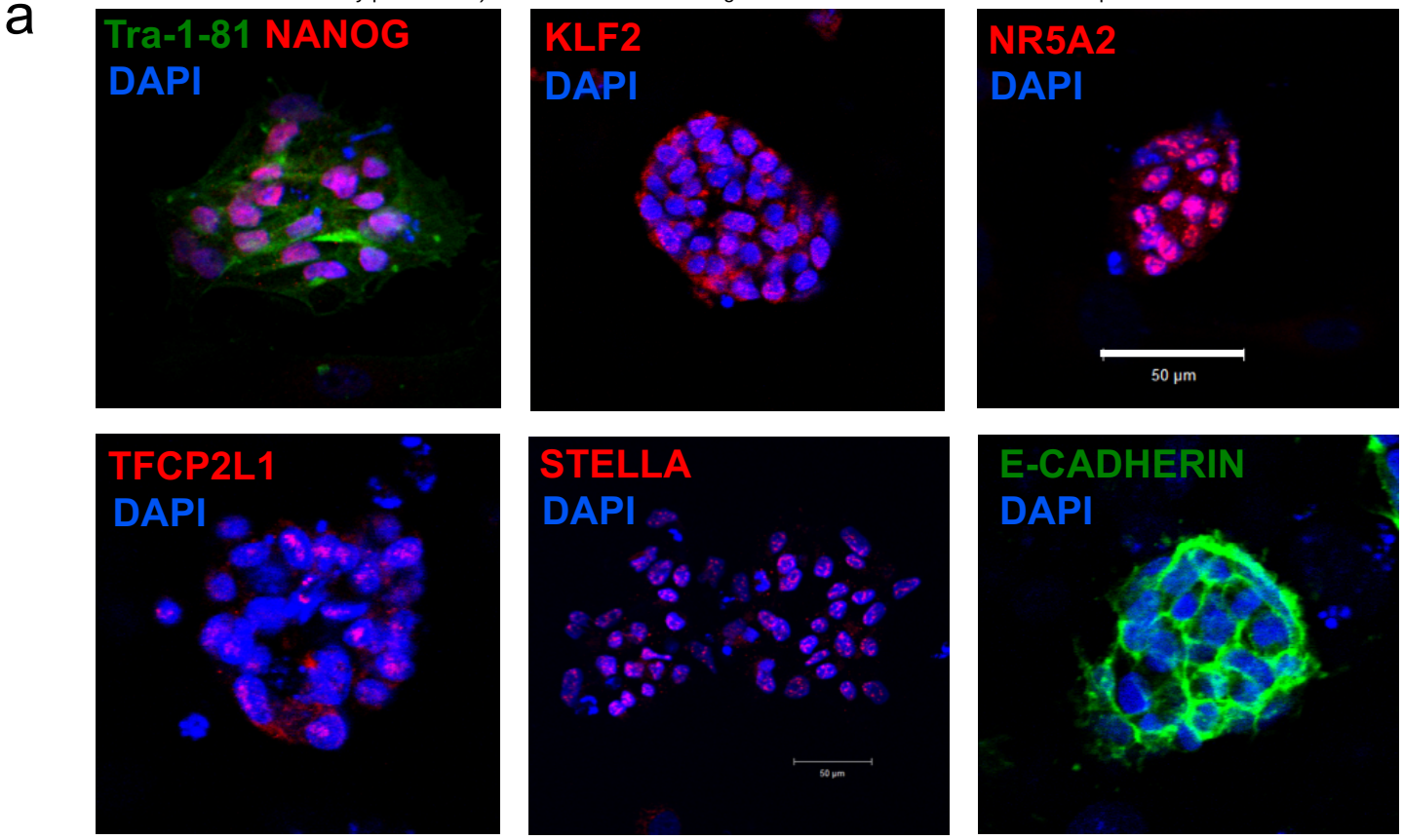

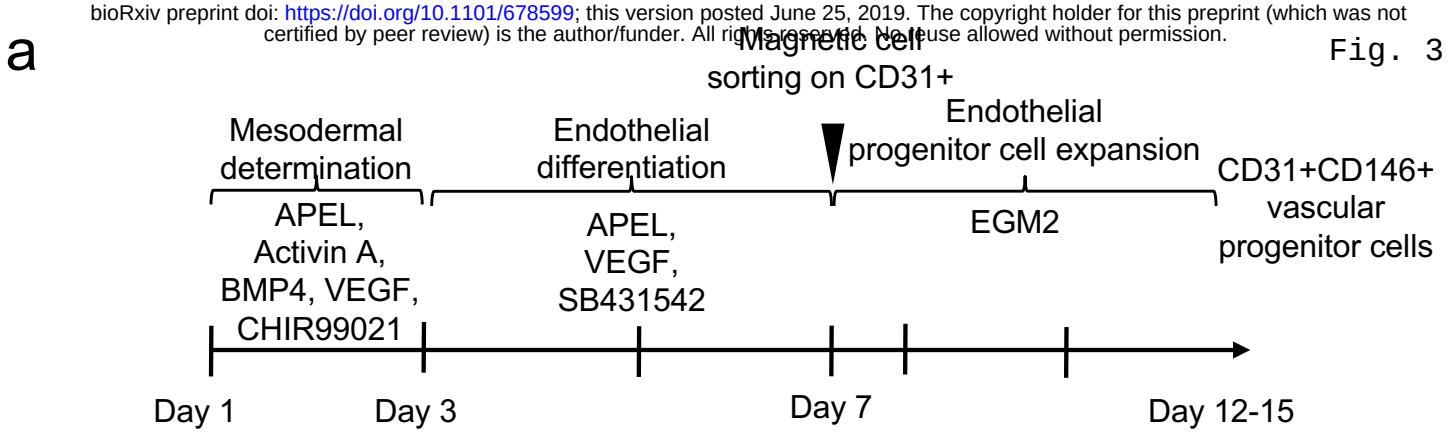

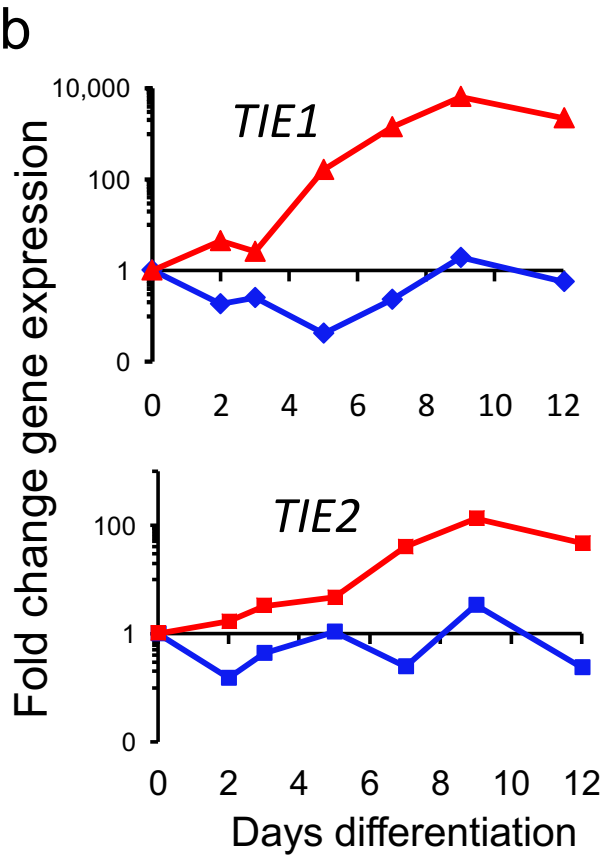

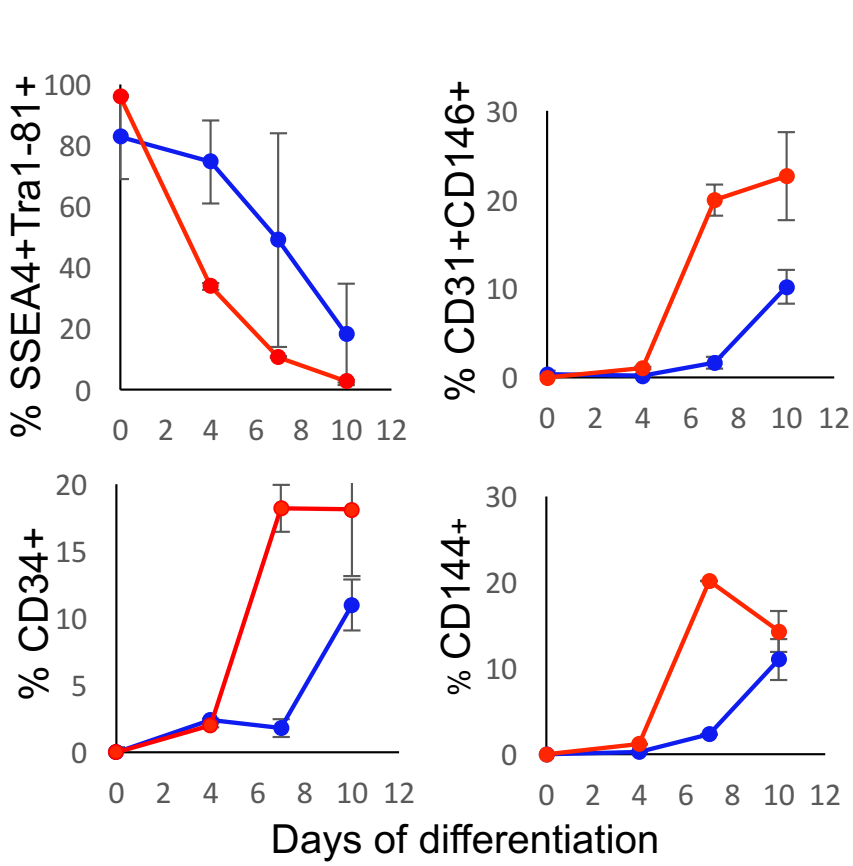

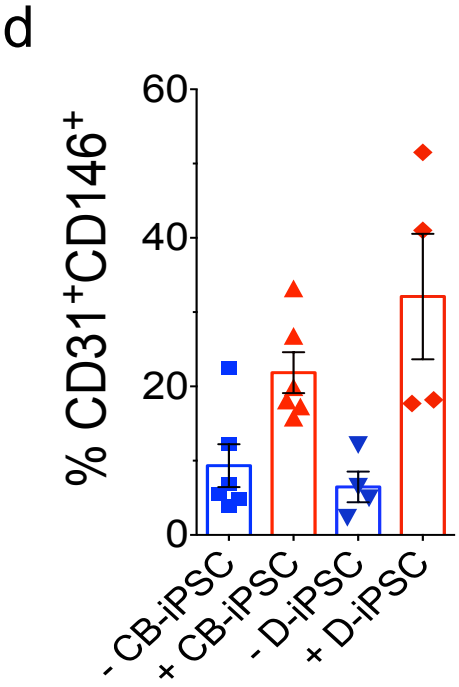

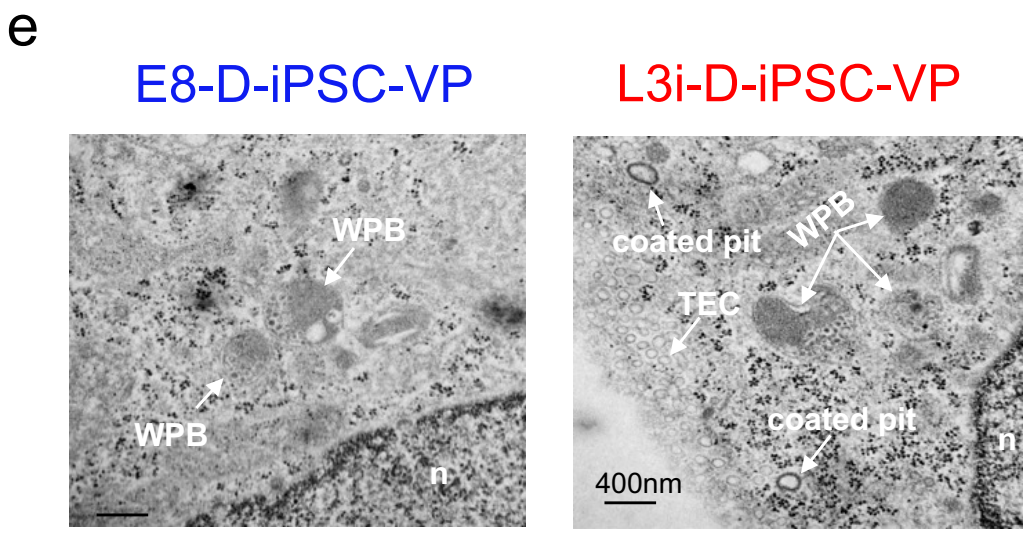

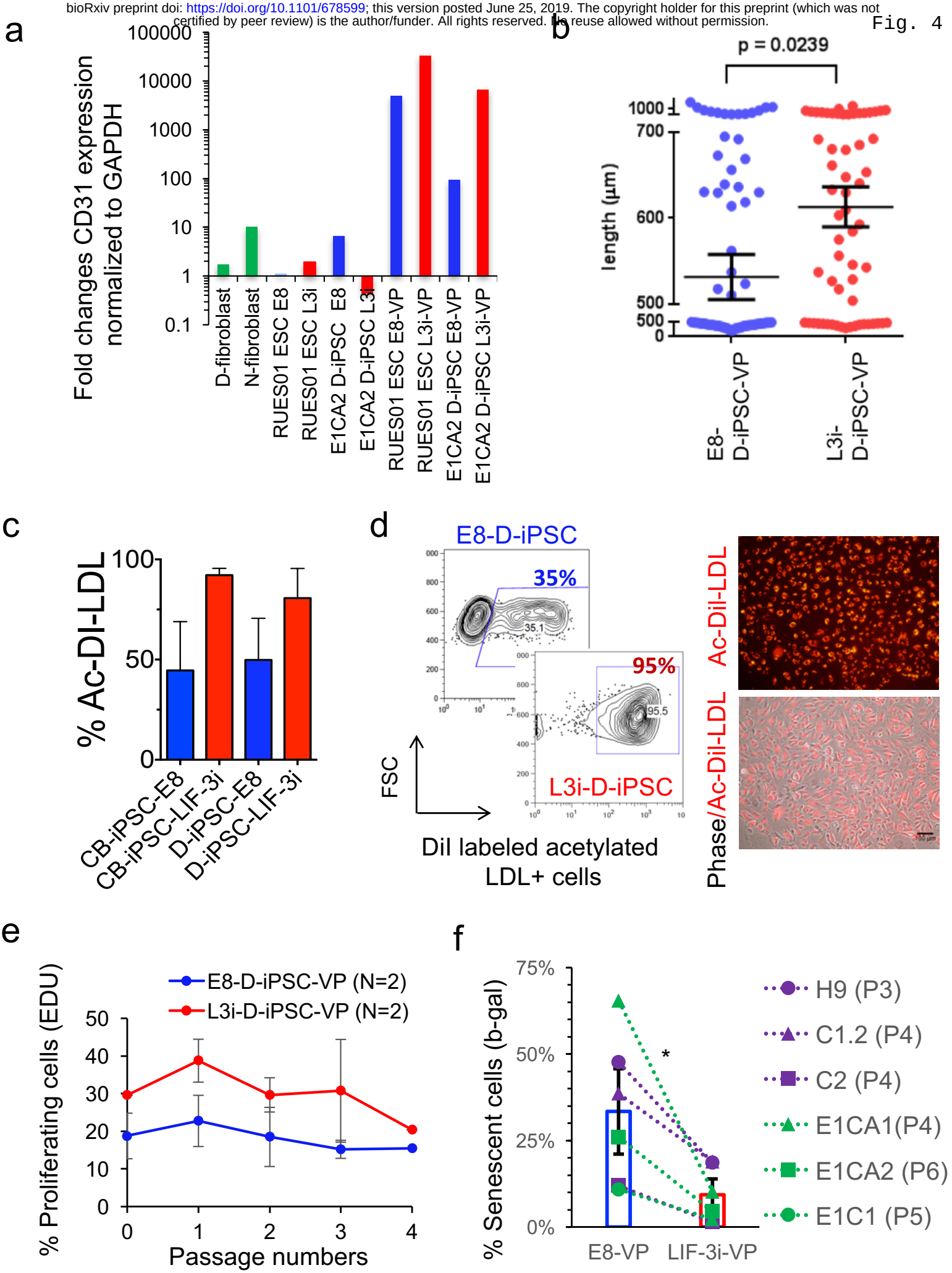

a

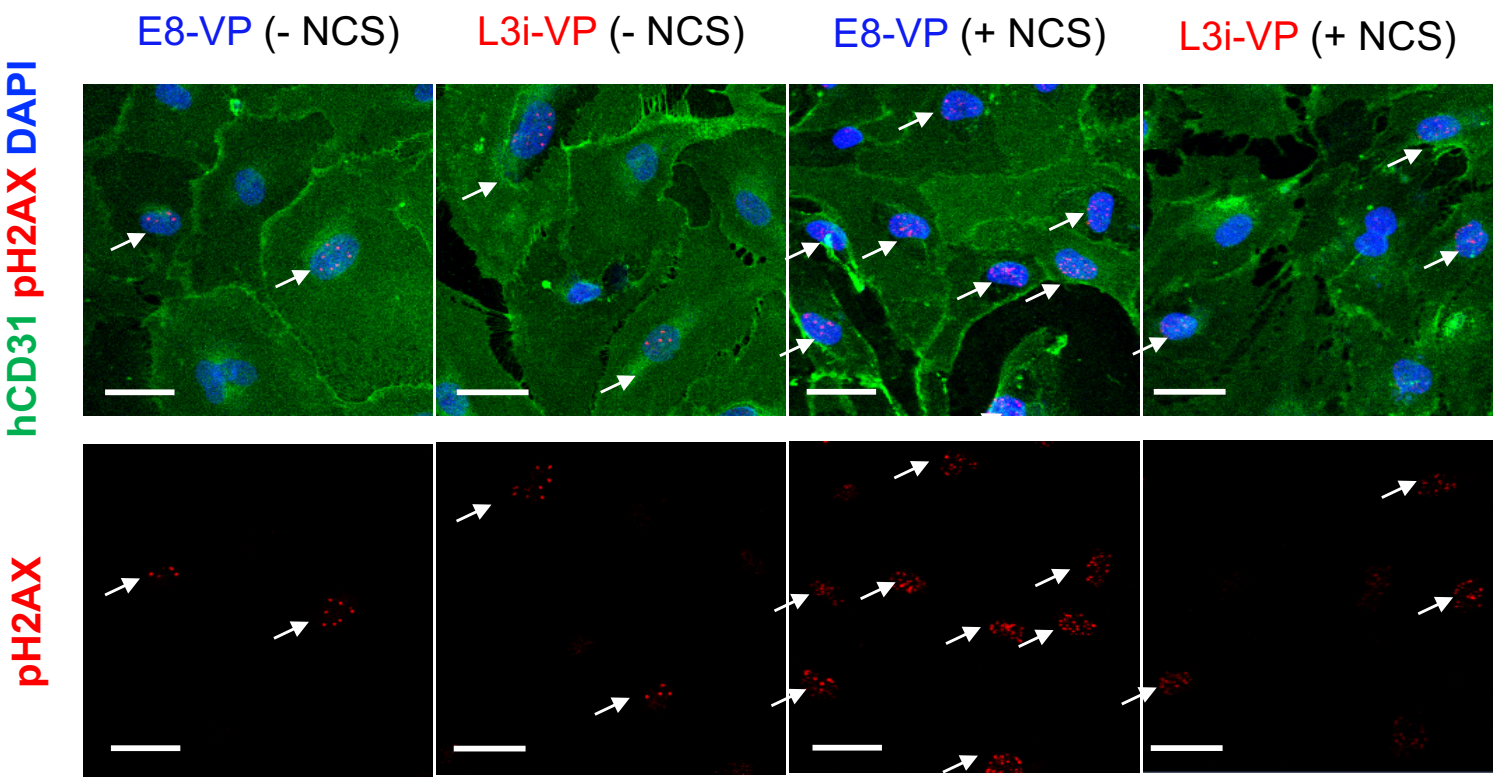

b

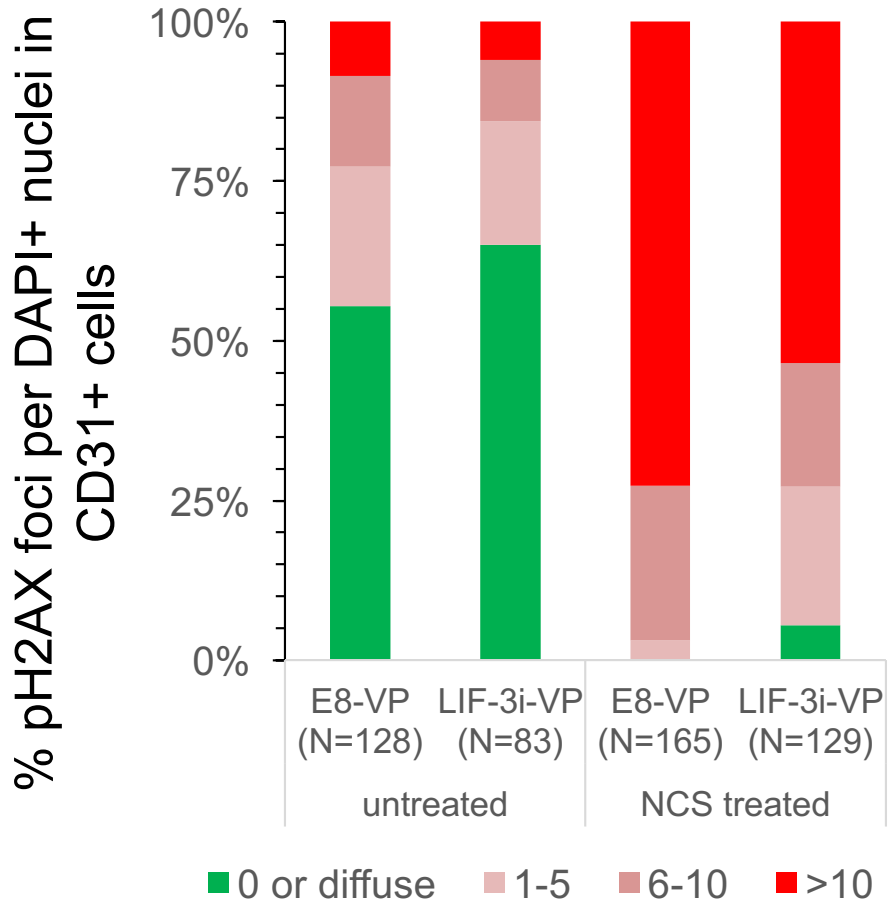

c

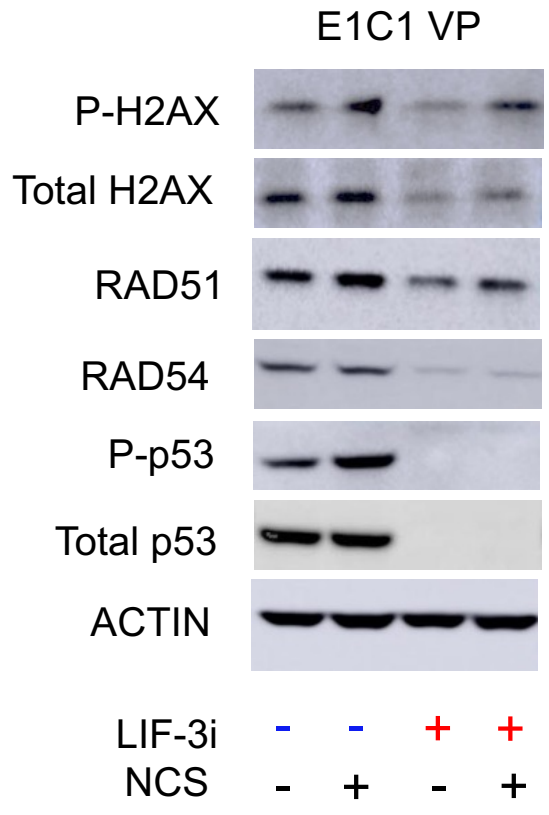

a

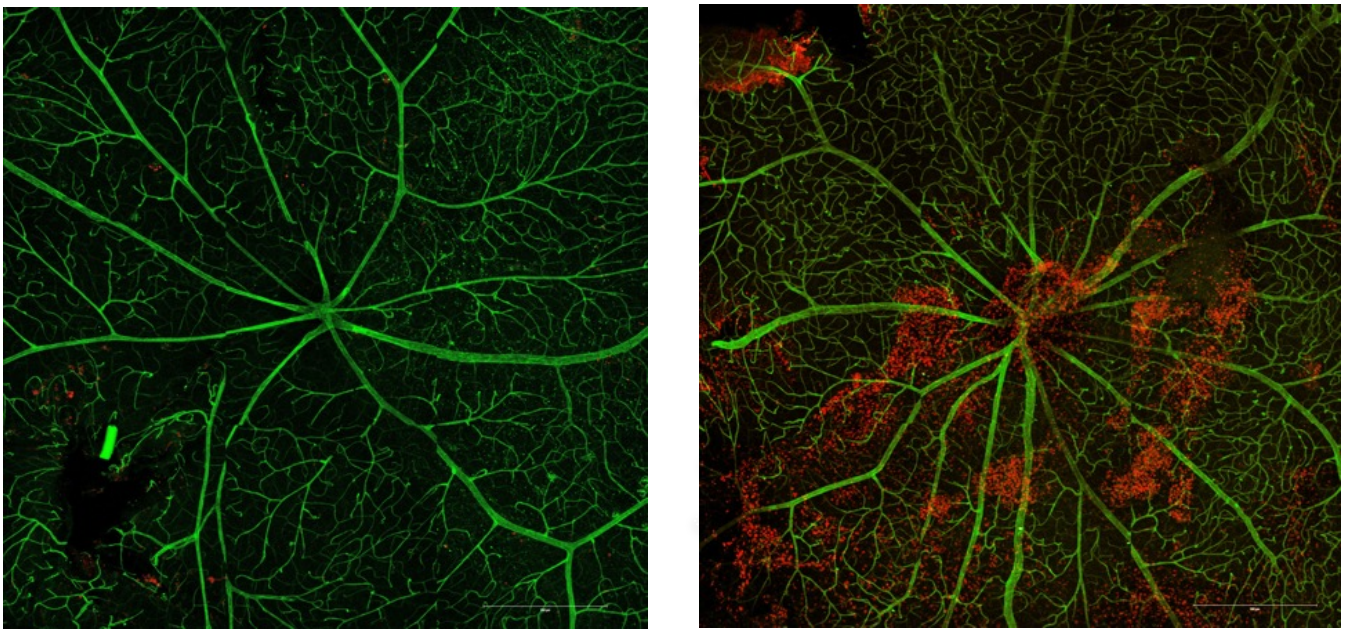

b

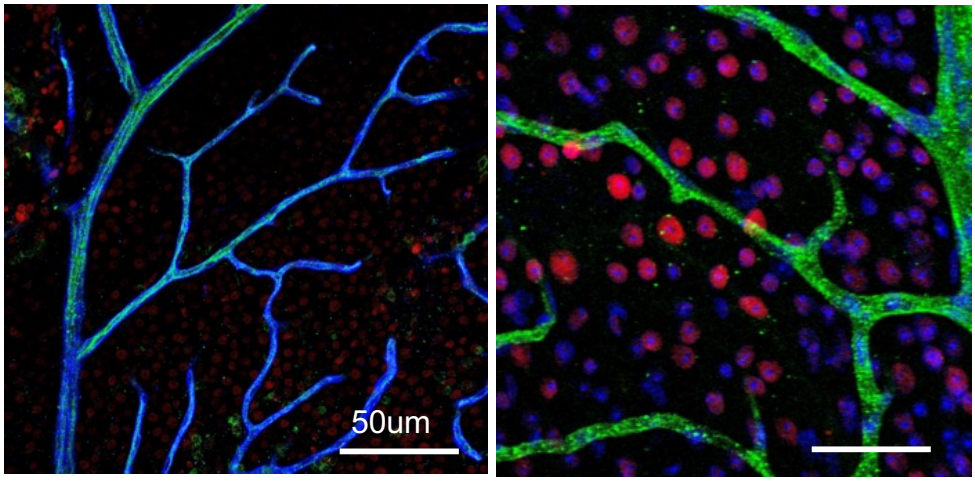

c

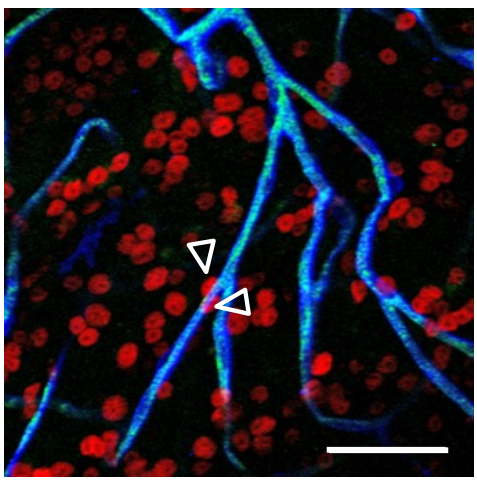

d

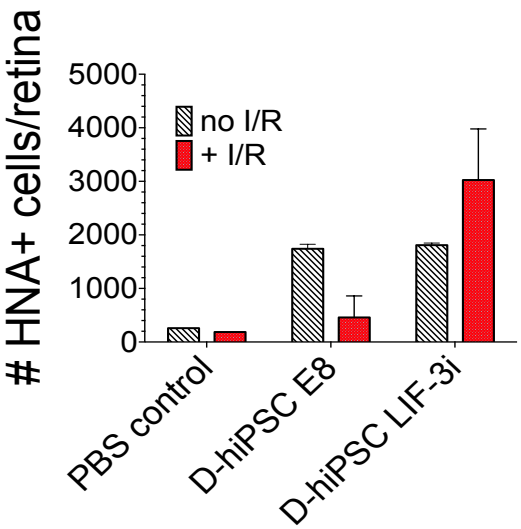

e

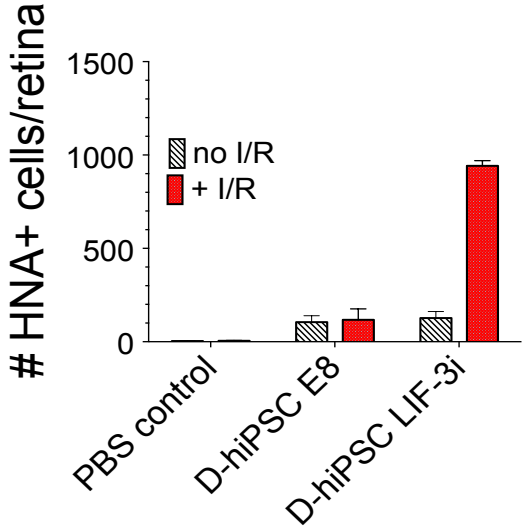

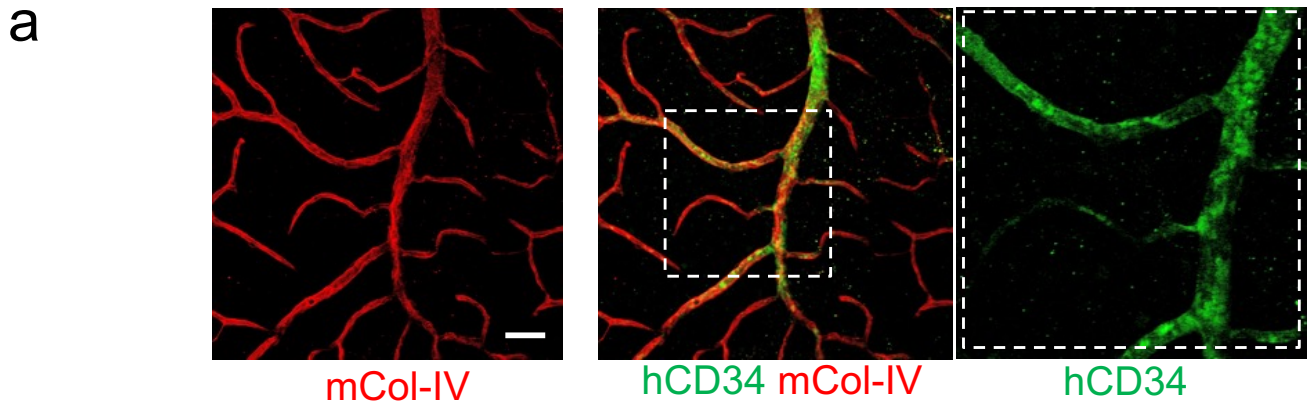
a
mCol-IV
hCD34 mCol-IV
hCD34

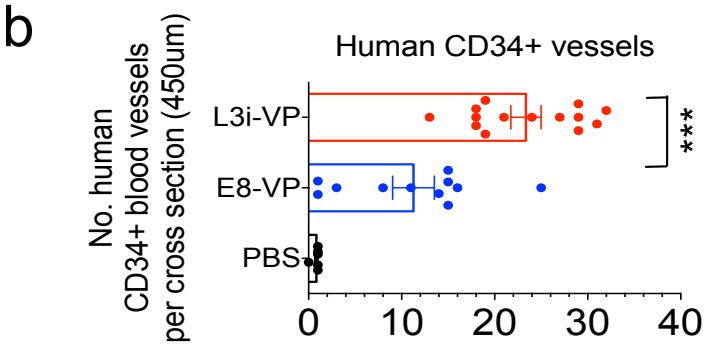
b
Human CD34+ vessels
No. human CD34+ blood vessels per cross section (450um)
L3i-VP
E8-VP
PBS
***
0
10
20
30
40

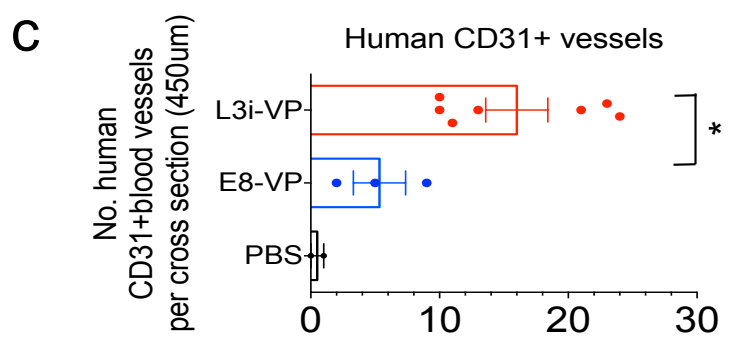
c
Human CD31+ vessels
No. human CD31+blood vessels per cross section (450um)
L3i-VP
E8-VP
PBS
*
0
10
20
30

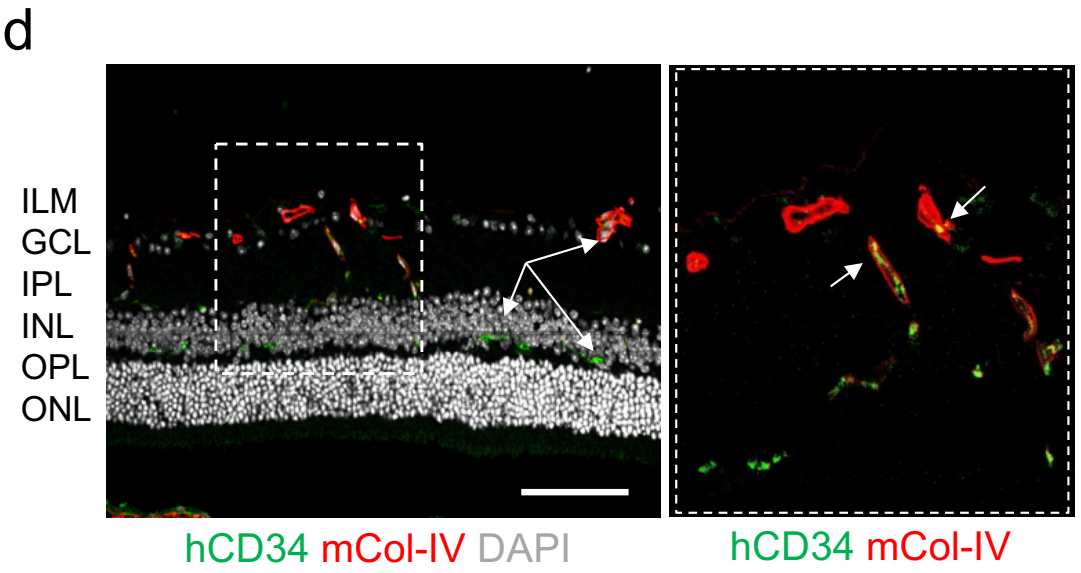
d
ILM
GCL
IPL
INL
OPL
ONL
hCD34 mCol-IV DAPI
hCD34 mCol-IV

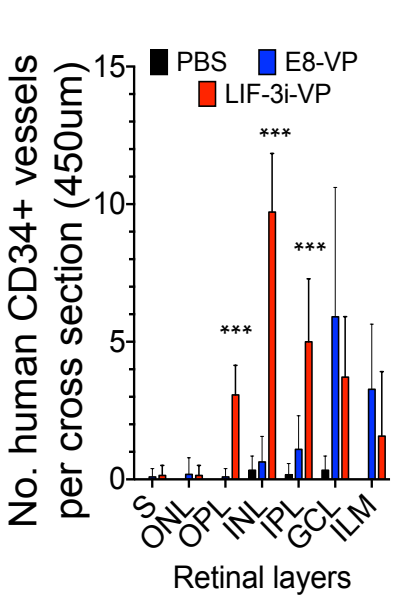
e
PBS
E8-VP
LIF-3i-VP
No. human CD34+ vessels per cross section (450um)
***
***
***
0
5
10
15
S
ONL
OPL
INL
IPL
GCL
ILM
Retinal layers

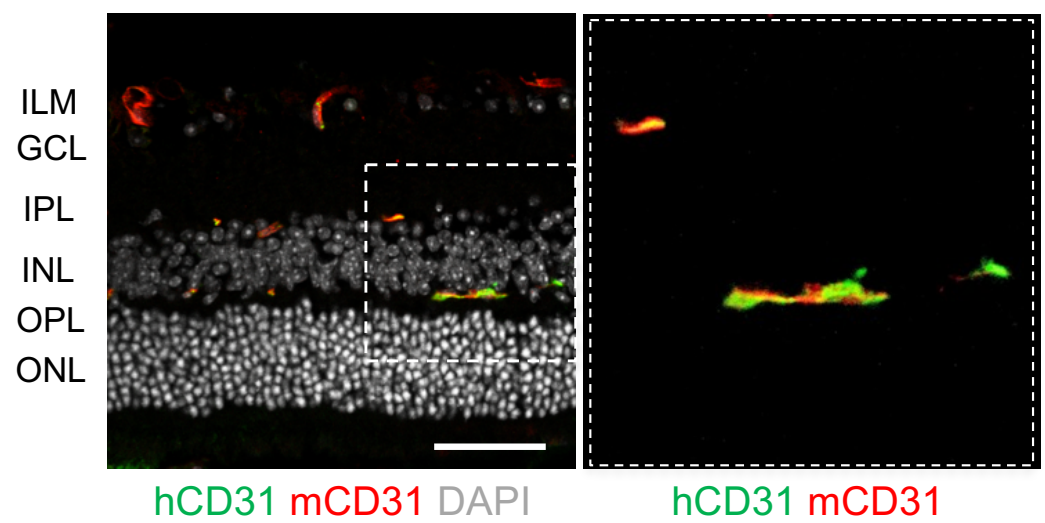
f
ILM
GCL
IPL
INL
OPL
ONL
hCD31 mCD31 DAPI
hCD31 mCD31

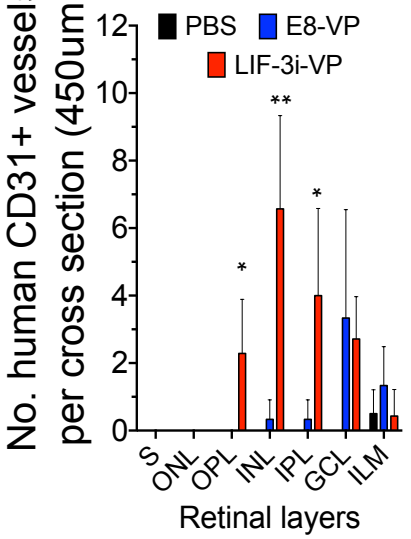
g
PBS
E8-VP
LIF-3i-VP
No. human CD31+ vessels per cross section (450um)
*
**
*
0
2
4
6
8
10
12
S
ONL
OPL
INL
IPL
GCL
ILM
Retinal layers

a

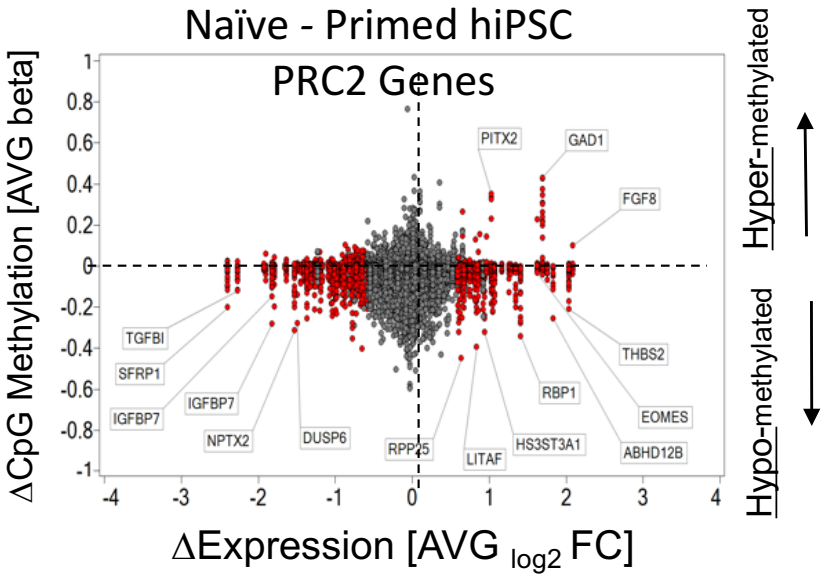

b

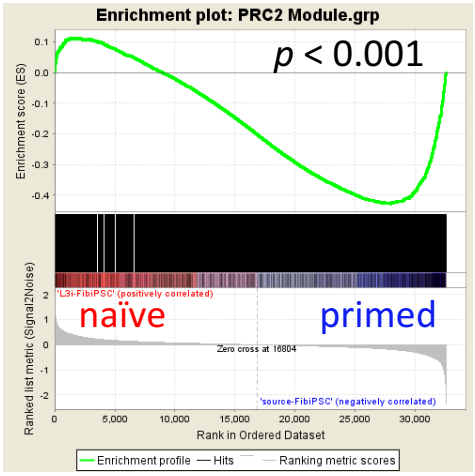

PRC2 genes- Fibroblast-hiPSC

c

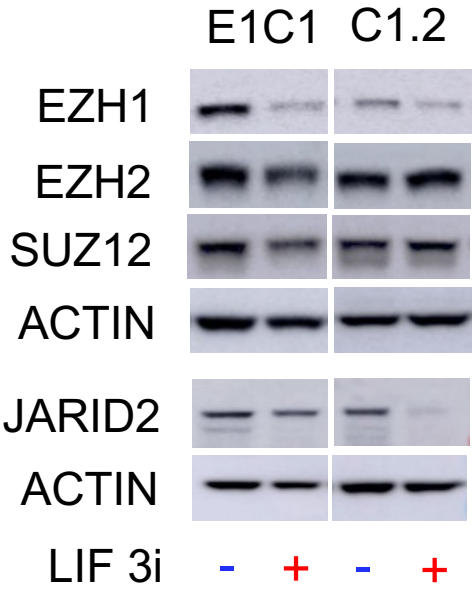

d

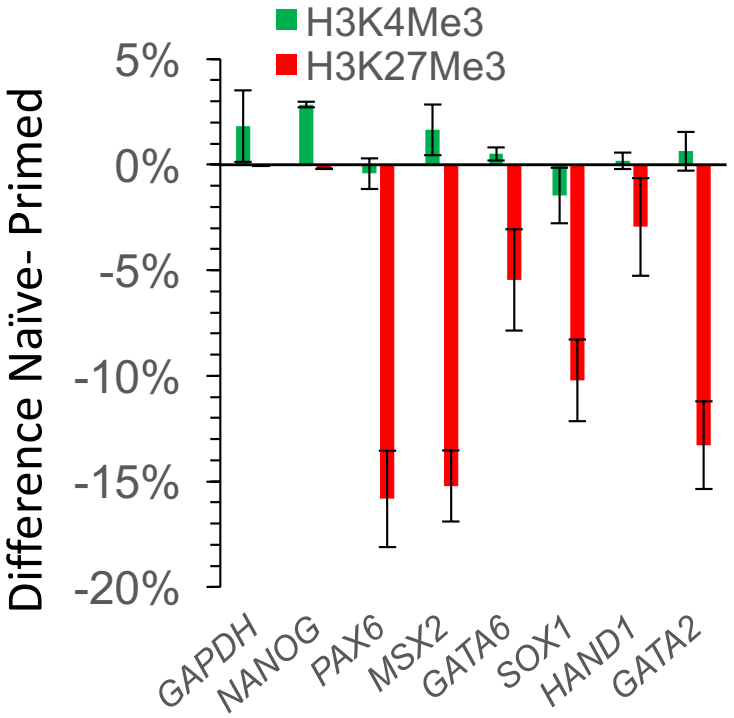

e

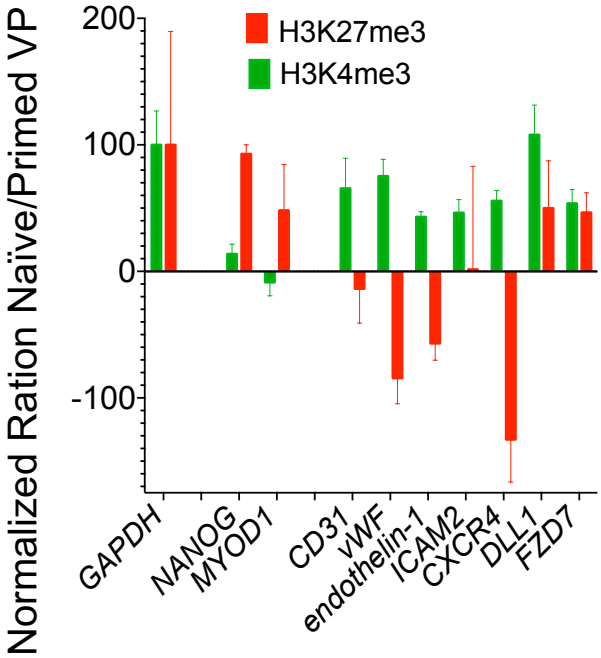

f